# A combined Eulerian-Lagrangian and thin film approximation model to investigate the disease-specific drug delivery efficacy on realistic lung geometry and breathing profiles

Sameer Kumar Verma[1,2] Saurabh Bhardwaj[3], Kishore Singh Patel[1a)*], B. Kiran Naik[1,2]

[1]Department of Mechanical Engineering, National Institute of Technology Rourkela, Odisha-769008

[2]Sustainable Thermal Energy Systems Laboratory (STESL), Department of Mechanical Engineering, National Institute of Technology Rourkela, Rourkela, Odisha - 769008

[3]Department of Applied Mechanics, Motilal Nehru National Institute of Technology Allahabad, Prayagraj -211004

[a)]Author to whom correspondence should be addressed: patelks@nitrkl.ac.in

## ABSTRACT

This study presents a computational assessment of antiviral liquid particle deposition in realistic human respiratory airways, comparing the actual inhalation cycle of a chronic obstructive pulmonary disease (COPD) patient to an ideal and healthy subject. Antiviral drugs are inhaled as fine droplets or mist, forming a thin liquid film along the airway walls of critical areas where respiratory viruses initially reside. The method employs an Eulerian-Lagrangian discrete phase model (DPM) to track individual droplet trajectories, and combines with an Eulerian wall film (EWF) model to predict the formation of the liquid coating upon droplet impact. This strategy overcomes the limitations of previous investigations that relied solely on DPM and ignored post-impact drug behavior. The patient-specific analysis focuses on airflow dynamics, deposition efficiency, and surface coverage for 1-10 μm particle sizes. It has been found that the large particles (10 μm) deposit primarily in the upper airways due to inertial impaction, while smaller particles (1-3 μm) reach deeper zones. The short and forceful breathings of COPD patients create complex asymmetric velocity distribution. As a result, even higher depositions are noticed along the upper airways (~5.28%) than the lower ones (~2.52%), limiting the drug penetration into deeper lung areas. For 10 μm particles, the maximal area coverage for the ideal (55.2%) and healthy (63.5%) profiles is on the left lower lobe, while in COPD, coverage shifts toward the carina (71.5%). These findings signify optimization efforts, such as breath-actuated inhalers and *pursed-lip breathing* for COPD patients to enhance drug delivery efficacy. The study illustrates the importance of patient-specific airway geometry and dynamic breathing profiles in enhancing respiratory treatment efficacy.

**Keywords:** Biofluid Dynamics, Pulmonary Fluid Mechanics, Drug Delivery, Patient-specific model, Discrete phase model, Eulerian wall film model

## I. INTRODUCTION

Respiration is essential for the physiological stability of the human body, preserving life and health. To ensure human well-being, it is critical to investigate the many processes involved in breathing, notably the deposition of inhaled particles. When airborne particles are inhaled, they can stick to the surfaces of the respiratory airways. This interaction can substantially impact health by allowing harmful pollutants to enter the respiratory system, potentially leading to pulmonary and cardiovascular disorders.[1] However, the respiratory system can also be used to transport medicinal substances. Inhaled drug particles are frequently employed in treating respiratory disorders, providing a direct and efficient method of administering drugs.[2, 3] Inhalation therapy is an efficient technique of respiratory drug delivery to cure various respiratory ailments, such as asthma, chronic obstructive pulmonary disease (COPD), etc. Figure 1(a) depicts the schematics of the major diseases caused by respiratory viruses and their infection mechanisms. The efficacy of drug delivery to specific airway sites is widely influenced by a range of factors, like the shape and size of drug particles, the physical conditions of the patient, and the choice of inhalation devices such as pressurized metered dose inhalers (pMDIs), nebulizers, and dry powder inhalers (DPIs) [Fig. 1(b)].[3, 4]

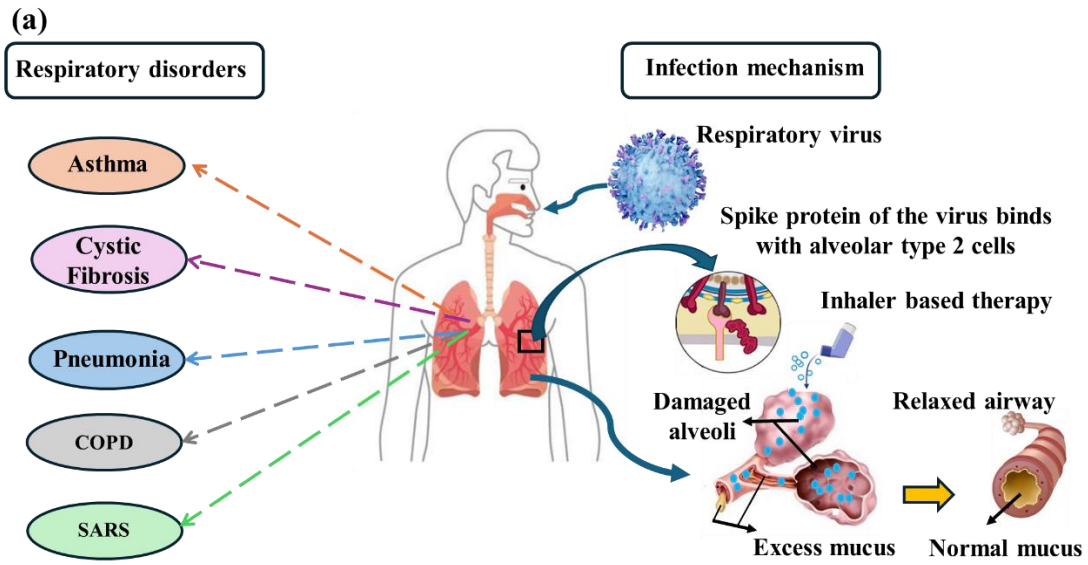

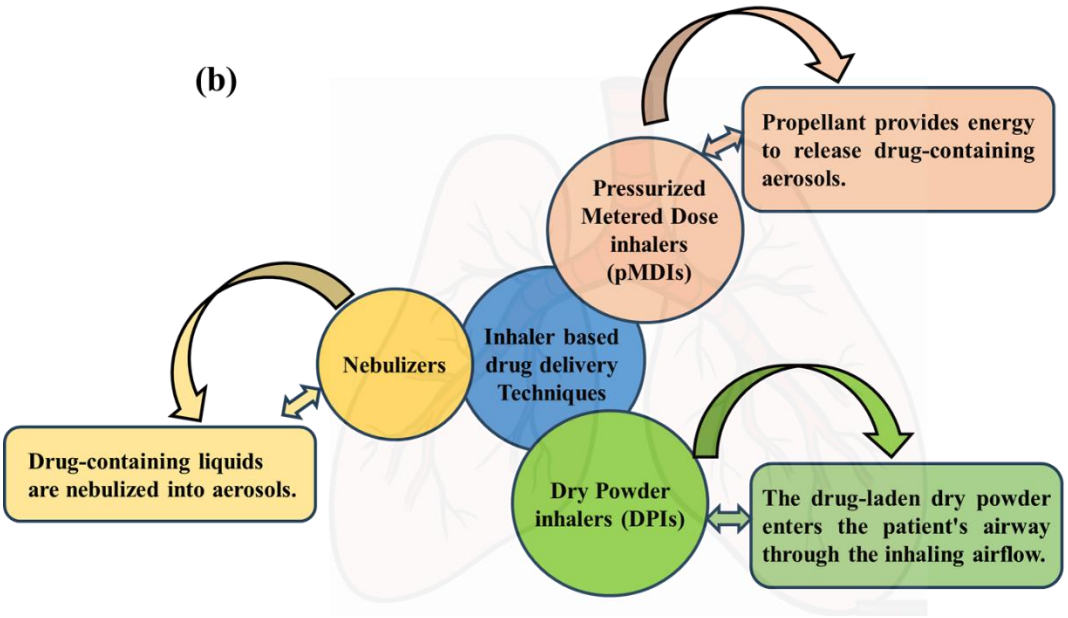


**FIG. 1.** Schematic representations to illustrate (a) the respiratory disorders and the infection mechanism of the respiratory virus that results in airway inflammation, alveolar damage, and increased mucus production and (b) different inhaler-based direct drug delivery approaches. The direct drug delivery methods are effective in neutralizing the pulmonary viruses.

Numerous experimental research and computational fluid dynamics (CFD) simulations have been carried out to predict the trajectory and deposition of drug particles in the human lung.[5–8] Weibel's geometry, often known as the ideal and symmetric lung geometry,[9] is helpful in understanding particle trajectory and deposition. Xu and Yu[10] performed a theoretical investigation based on Weibel's model for up to generation 23 (G23) to evaluate the effect of age on aerosol deposition for various particle sizes. Comer *et al.*[11] used Weibel's model to replicate particle deposition patterns between G3 and G5. Using a simplified human respiratory tract model, Rahman et al.12 investigated the depositions of 5, 10, and 20 μm particles for the people of 50, 60, and 70 years age groups. They reduced airway diameter by 10% for each 10 years of age rise. The study discovered that aging affects deposition efficiency, with particles accumulating more in the upper respiratory tracts in 70-year-olds than in 50-year-olds lungs, and the escape rate of the particle decreases with age. Moreover, Rahman et al.[13] also investigated the deposition of nano-sized particles of 5, 10, and 20 nm up to G11 using a simple lung airway model. They discovered that 5 nm particles had much greater deposition efficiency in each generation than the 10 and 20 nm particles. Verma *et al.*[14] have done a computational analysis of Weibel's geometry (G0-G4) to calculate the more realistic particle deposition by employing the discrete phase model (DPM) and Eulerian wall film (EWF) approach. The above

literature demonstrates that CFD is a robust tool for estimating the airflow and particle dynamics inside the respiratory tract.

Further studies have extended the analysis of particle deposition dynamics to patient-specific human lung geometries, offering deeper insights into airflow behavior and deposition patterns in the airways.[15–17] Oakes *et al.*[18] examined airflow across various developmental stages, adults, children, and infants, to better understand age-dependent flow dynamics. Beni *et al.*[19] used a realistic lung model to analyze severe acute respiratory syndrome (SARS) virus deposition patterns under varying constant flow rates and aerosol sizes, although their study was confined to the nasal cavity and trachea without extending into the deeper lung generations. Taheri *et al.*[20] reconstructed a human airways model from computed tomography (CT) scans to explore how swirling inlet conditions and different particle release strategies affect deposition efficiency. Wedel *et al.*[21] compared steady-state simulation results with transient shear stress transport (SST) k-ω and detached eddy simulation (DES) models to evaluate particle deposition behavior in CT scan-based male and female lung geometries. The study considered various particle size distributions representing different respiratory activities, such as coughing, sneezing, and normal breathing. Islam *et al.*[22] analyzed the transport and deposition of SARS-CoV-2 virus particles in a CT scan G17 lung model, focusing on their movement toward the terminal airways. Additionally, several researchers [23, 24] have examined the transport of microplastics through the airways and their deposition on lung surfaces in realistic lung models using a Lagrangian-based approach.

All previous investigations applied a constant breathing rate as an inlet condition. However, during drug inhalation, the rate at which airflow reaches the lungs through the mouth varies in a cyclical pattern rather than remaining constant. Some studies have considered transient airflow in the human lungs.[25–31] Paul *et al.*[32] replicated the deposition of cigarette smoke particles in patient-specific human lung airways extending up to the G6 of airway bifurcations, including a realistic inhalation profile. Naseri *et al.*[33] employed a sinusoidal airflow rate to investigate the path of microparticles traveling from the nostrils to the trachea. The study examined two different inhalation conditions, rest and moderate, allowing for analysis of how varying respiratory patterns influence particle transport. Makris *et al.*[34] adopted a sinusoidal airflow rate with two frequencies normal and high, to model airflow and particle deposition between generations G3 and G4. Tiwari *et al.*[35] employed a transient inhalation profile through a DPI to predict particle deposition in the G6 lung airways model. Bhardwaj *et al.*[16]

computationally examined how the transient motion of glottal structures affects inhalation therapy using a realistic airway geometry under a DPI inhalation profile. Their results revealed that glottal deformation in the conducting airways significantly influences the localized deposition of smaller micron-sized particles. Grgnic *et al.*[36] displayed that deposition efficiency changes between transient and continuous flow patterns. They employed an escalating flow of 45 liters per minute (LPM), followed by a rapid deceleration to zero.

Numerous research studies have investigated breathing mechanics and particle deposition in the lungs using a DPM-based approach. However, the typical DPM technique has limitations in capturing post-impact particle behavior, such as the extent of surface coverage and the thickness of the film deposited by the tiny liquid droplets. The previous simulation models were also inadequate in predicting other post-impact dynamics, such as the spread of the drug layer due to the shearing effects of the bulk air medium in breathing. To address these gaps, this study combines the thin-film approximations model with the traditional Eulerian-Lagrangian discrete phase tracking model. This approach comprehensively analyzes drug particle depositions with precise information on deposition locations and comprehensive area coverage.

Along with the state-of-the-art computational method, further novelty lies in investigating the impact of patient-specific realistic breathing against both idealistic and realistic breathing of a healthy adult lung. It has been observed that a patient suffering from an acute case of COPD has a shortened and forceful breathing pattern. This significantly affects the overall airflow dynamics and deposition behavior of the inhaled drug particles. This work investigates the detailed impact of changes in breathing patterns on a CT-scanned realistic airways domain up to the (G7). Hence, this work highlights the implications of employing a coupled DPM and EWF model on realistic breathing profiles and lung airways to improve the accuracy of pulmonary drug delivery predictions.

## II. METHODOLOGY

The mechanisms that cause particle deposition in the respiratory tract are impaction, diffusion, interception, and sedimentation.[37, 38] The effectiveness of each mechanism is influenced by factors such as airway geometry, particle properties (e.g., size, shape, and density), and the breathing rate. Overall, impaction and sedimentation mechanisms primarily regulate microparticle deposition inside the lungs. The numerical method is comprised of two sections:

an airflow model that mimics airflow within the human airways and a particle transport model that predicts particle movement based on airflow velocity. The present analysis is performed using ANSYS FLUENT software (2023 R2).

**A. Conceptualization of the Study**

Figure 2 depicts the conceptual framework for the current research investigation. The DPM is a popular tool for simulating the motion and interactions of discrete particles inside bulk fluid flows. DPM, which captures the interactions between particles and the surrounding fluid, allows tracking of an individual particle using a Lagrangian approach while precisely accounting for drag and gravitational forces. However, this study does not account for other forces such as Saffman's lift force, Brownian force, virtual mass force, electrostatic force, or thermophoretic force. Furthermore, the creation of a thin liquid film due to the impact of microsized droplets and their coalescence is modeled using EWF approximations, which are identical to the lubrication approximations used in thin film dynamics. This technique is an alternative to volume-of-fluid multiphase approaches, which otherwise necessitate an extremely fine mesh near the wall to capture thin film behavior and implicate higher computing costs. In addition to modeling thin film development, coupling DPM with Eulerian approximations enables the tracking of secondary particles formed by splashing, stripping, and separation processes.[39] The salient features of our investigation are as follows:

- The current study evaluates the effects of airflow velocity and vorticity distribution inside the CT scan-based respiratory airways under healthy and diseased realistic breathing maneuvers.
- A comprehensive examination assesses deposition properties such as film thickness, area coverage, and deposition efficiency by altering particle sizes (1-10 μm) and three breathing cycles (ideal, healthy, and COPD).
- The objective is to examine particle deposition patterns across several airway lobes and compare the deposition patterns along the left and right lungs using diseased, idealistic, and realistic healthy breathing profiles.

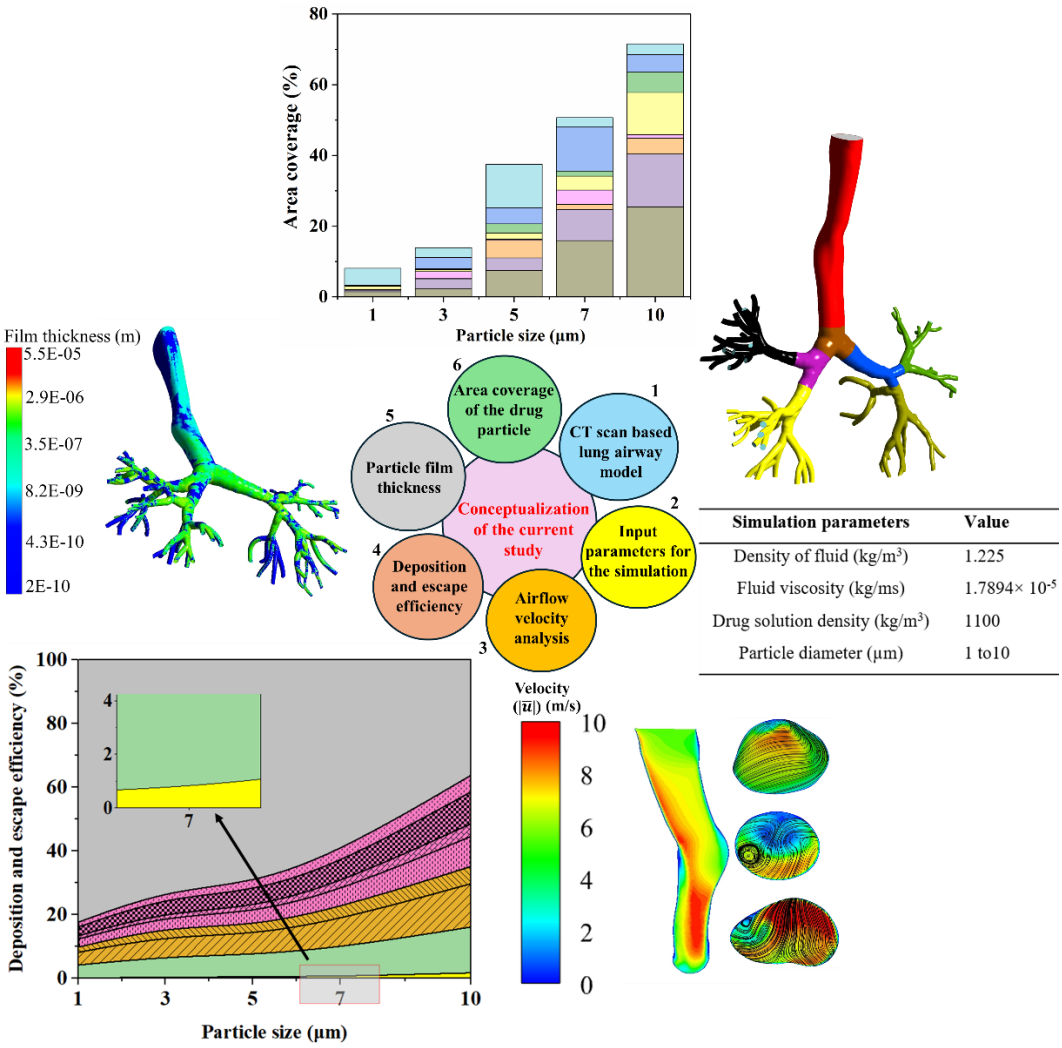


**FIG. 2.** A comprehensive workflow exhibiting drug particle dynamics in a CT-based lung model, emphasizing variations across particle sizes. The simulation incorporates airflow behavior and wall interaction effects to access inhalation drug delivery efficacy.

## B. Respiratory tract model

This study presents a three-dimensional anatomical lung model of a healthy adult male created using CT scan data. In this investigation, we employ the SimInhale benchmark anatomical model of the respiratory system, which was initially developed by Lizal *et al.*,[40, 41] and used further by Koullapis *et al.*[42] and Bhardwaj *et al.*[16] The tracheobronchial model spans from the trachea to the G7 with different lobes as the right lobe (RL), right upper lobe (RUL), right lower lobe (RLL), left lobe (LL), left upper lobe (LUL), and left lower lobe (LLL), as shown in Fig. 3(a). The locations of the cut-planes for the airflow analyses are depicted in Fig. 3(b). These defined planes aid in determining the accuracy of numerical simulations by confirming flow characteristics in various airway sections.

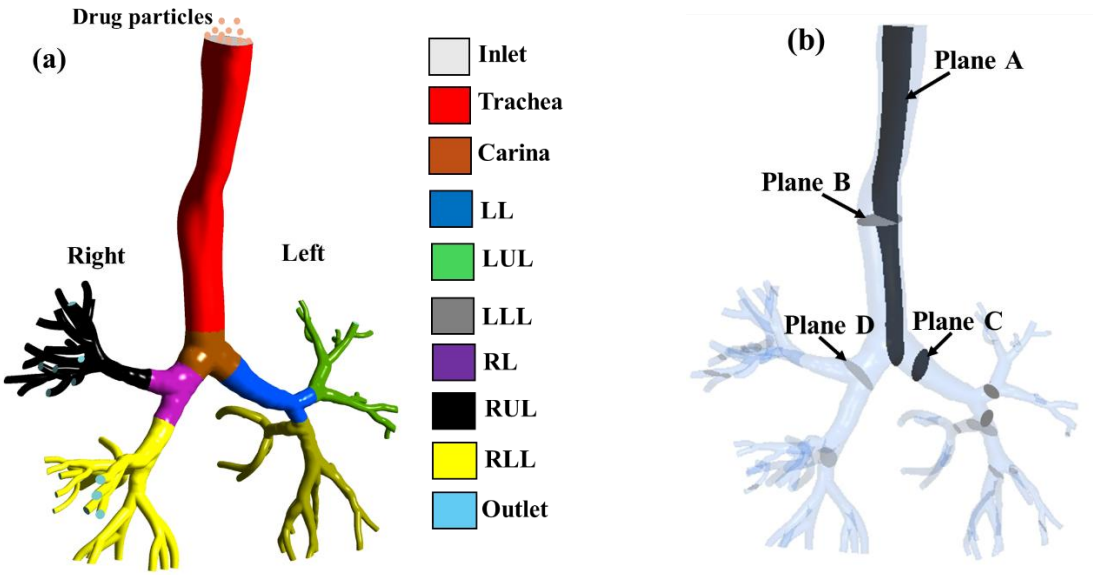


**FIG. 3.** Lung airway model with different cut-sectional planes. (a) A CT-scan-based model of the bronchial airway up to G7.[42] The color tagging on this model illustrates several lobar areas and drug particle entry through the trachea. (b) The location of the cut-sectional planes at which the airflow parameters are investigated.

### C. Airflow model

Since air is the working fluid in this study, it is assumed to behave as a Newtonian and incompressible.[43] Furthermore, the typical inlet Reynolds number ranges between 1900 (for ideal breathing) to 5702.73 (for COPD breathing). The dynamics of airflow inside the lung are characterized by the Reynolds-averaged Navier-Stokes (RANS) equations,

Mass conservation:

$$\frac{\partial u_i}{\partial x_i} = 0 \tag{1}$$

Momentum conservation:

$$\frac{\partial u_i}{\partial t} + u_j \frac{\partial (u_i)}{\partial x_j} = -\frac{1}{\rho}\frac{\partial p}{\partial x_i} + \frac{\partial}{\partial x_j}\left[(\vartheta + \vartheta_T)\left(\frac{\partial u_i}{\partial x_j} + \frac{\partial u_j}{\partial x_i}\right)\right] \tag{2}$$

where, $\rho$ denotes the density of the air, $\vartheta$ and $\vartheta_T$ represent the coefficients of kinematic molecular and turbulent viscosity, respectively. The SST *k-ω* turbulence model was used in this work to improve modeling accuracy. The transport equations for turbulent kinetic energy (*k*), and specific dissipation rate *(ω)* can be expressed by,

$k$ equation:

$$\frac{\partial k}{\partial t} + u_j \frac{\partial k}{\partial x_j} = \tau_{ij} \frac{\partial u_i}{\partial x_j} + \frac{\partial}{\partial x_j}\left((\vartheta + \sigma_k \vartheta_T)\frac{\partial k}{\partial x_j}\right) \tag{3}$$

$\omega$ equation:

$$\frac{\partial \omega}{\partial t} + u_j \frac{\partial \omega}{\partial x_j} = \alpha \frac{\omega}{k} \tau_{ij} \frac{\partial u_i}{\partial x_j} - \beta \omega^2 + \frac{\partial}{\partial x_j}\left((\vartheta + \sigma_\omega \vartheta_T)\frac{\partial \omega}{\partial x_j}\right) \tag{4}$$

where, $\tau_{ij}$ represent the viscous stress tensor. Further, the turbulent kinematic viscosity can be approximated empirically as $\vartheta_T = \frac{C_\mu f_\mu k}{\omega}$, and the function $f_\mu$ represents as $f_\mu = exp\left[-3.4/\left(1 + \frac{R_T}{50}\right)^2\right]$ with $R_T = \frac{\rho k}{\mu \omega}$. The additional constants in the above equations are defined as:

$\alpha = 0.555$, $\beta = 0.8333$, $C_\mu = 0.09$ and $\sigma_k = \sigma_\omega = 0.5$.

The pressure-velocity coupling is done by a SIMPLE algorithm, while the governing equations for momentum, turbulent kinetic energy, and specific dissipation rate are discretized using a second-order upwind scheme. The convergence criteria for all equations are set to $10^{-6}$ to ensure numerical accuracy and solution stability.

**D. Breathing profile**

A realistic breathing cycle was replicated by implementing a time-varying inlet condition. (Fig. 4). We employed the inhalation profile of a COPD patient with severe airway occlusion, as described by Colasanti *et al.*[44], to simulate compromised breathing. However, no artificial narrowing was applied to the airway segmentation because such obstructions usually occur downstream in the smaller airways (higher generations), which were not modeled in the current study and are not visible in segmentations.[44, 45] The diseased inhalation profile of COPD shown in Fig. 4 closely resembles the profile described by Vitacca *et al.*[46] for people with COPD recovering from exacerbation. The peak inspiratory flow rate of the breathing waveform is 0.96 liters per second (L/s). A healthy breathing profile (Fig. 4) was obtained from the clinical measurements shown by Scheinherr *et al.*[47], which has been used further for healthy breathing inlets. The peak inspiratory flow rate of the breathing waveform is 0.82 L/s. An idealized waveform is created from sinusoidal functions representing tidal breathing.[48] Based on this, we reconstructed the inhalation profiles of a 25-year-old individual with a peak flow rate of 0.36

L/s. Zero gauged pressure is imposed at all outlets, and walls of the airways are considered no-slip and stationary.

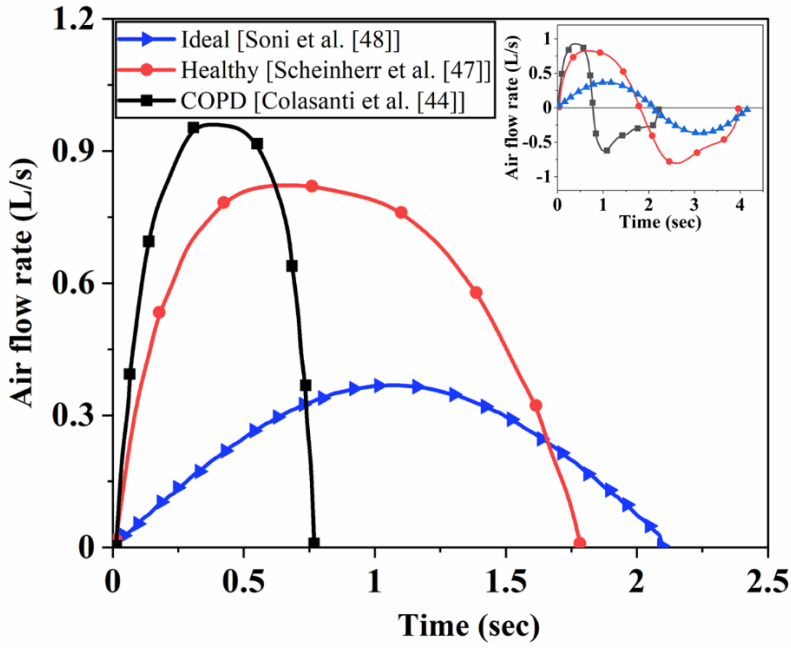


**FIG. 4.** The comparison of inhalation airflow profiles for ideal, healthy, and COPD conditions during the inspiratory phase, focusing on disease-induced differences in peak flow rate and breathing time. The inset small plot shows complete breathing cycles, including exhalation.

### E. Particle transport

A one-way coupling is employed between the continuous (air medium) and the discrete (liquid particles) phases, and the volume concentrations of particle release are kept below 0.1%.[16] Many studies have neglected particle-particle interactions, as the particle suspension becomes sufficiently diluted upon reaching the pulmonary airways.[17] Thus, the current model employs a one-way coupling approach, in which particle motion is driven by airflow dynamics while the effect of particles on the airflow is neglected.[49] In this study, we use the DPM-EWF to examine the interactions between continuous and discrete phases.

#### *1. Discrete phase model (DPM)*

The Eulerian-Lagrangian DPM approach is implemented to simulate the trajectories of the particles within the lung airways. Particles are introduced from a surface upstream of the airway entrance to ensure sufficient dispersion before entering the trachea. Unlike the continuous phase, particles in DPM are not treated as a continuous medium. Instead of solving a transport

equation for them, each particle's trajectory is computed individually in the Lagrangian frame of reference by solving its equation of motion, allowing for detailed tracking of particle behavior throughout the domain. The equation is stated as follows: [50]

$$\frac{\partial u_p}{\partial t} = F_D\left(u - u_p\right) + \frac{g(\rho_p - \rho)}{\rho_p} + S \tag{5}$$

where, $F_D\left(u - u_p\right)$ reflects the drag force per unit mass on the drug particles, and the last term accounts for the gravitational force.

The $F_D$ can be further expressed as,

$$F_D = \frac{18\mu C_D Re_p}{\rho_p d_p^2\, 24} \tag{6}$$

where, $u$ indicates the velocity of air, $u_p$ signifies the drug particle velocity, $\rho$ denotes the density of the air, μ is the dynamic viscosity of air, $\rho_p$ and $d_p$ symbolizes the density and diameter of the drug particle, respectively, and $C_D$ represents the drag coefficient.

Relative particle Reynolds number ($Re_p$) is given by

$$Re_p = \frac{\rho d_p |u_p - u|}{\mu} \tag{7}$$

In Eq. (5), the variable $S$ represents the additional forces that can influence particle motion under specific conditions. These forces are Saffman's lift force, Brownian force, virtual mass force, and thermophoretic force. Thermophoretic force is neglected in this study due to the lack of a temperature gradient. Brownian force is relevant in laminar flows with sub-micron particle sizes and is negligible within the current Reynolds number range. The virtual mass force becomes significant when the carrier phase (air) density greatly exceeds the discrete phase density $\left(\frac{\rho}{\rho_p} >> 1\right)$; however, this assumption does not hold for the present investigation, rendering this force insignificant. Saffman's lift force, caused by shear, significantly affects sub-micron particles but is excluded here as the particle diameters range from 1 μm to 10 μm. Consequently, only drag and gravitational forces are considered significant in the present analysis.[51] A stochastic tracking method was employed to capture the fluctuations in the turbulent flow field during simulation with the discrete random walk model and a random eddy lifetime. These components are defined under the turbulent dispersion parameters, which enable a more realistic modeling of particle trajectories inside the fluctuating turbulent flow field. Furthermore, particles reach the computational domain via the inlet surface. For particle

deposition, a "trap" boundary condition is applied to the airway walls, indicating a zero coefficient of restitution, meaning there will be no rebound of the particles, while an "escape" boundary condition is applied at outlets.[52] The escape condition allows particles to exit through the outlet without being reflected. Under this trap boundary situation, the tiny droplets adhere to the airway walls, forming a thin layer of drug solution coatings. The dynamics of these thin drug layers are further investigated using the EWF model.

***2. Eulerian wall film (EWF) model***

The film model represents a two-dimensional thin liquid film on a wall surface. This thin film forms when liquid particles strike a solid surface within the domain. Upon impact, several outcomes are possible, such as the stick, rebound, spread, and splashing of the drug particles.[53] Out of all these, the current study has considered the *spreading* and *splashing* of the droplets, which allow the formation of a thin liquid coating and the formation of secondary droplets upon impaction. Furthermore, EWF coupling with Lagrangian and Eulerian-Eulerian multiphase solvers is possible. The fundamental assumptions of the EWF model suggest that the film consistently flows parallel to the surface, which implies that the normal component of the film velocity is zero.[14]

The governing equations of the EWF model are given as [39]

$$\frac{\partial \rho_l h}{\partial t} + \nabla_s.(\rho_l h \vec{V}_l) = \dot{m}_s \tag{8}$$

$$\frac{\partial \rho_l h \vec{V}_l}{\partial t} + \nabla_s.(\rho_l h \vec{V}_l \vec{V}_l + \vec{D}_v) = -h\nabla_s P_L + \rho_l h g_\tau + \frac{3}{2}\vec{\tau}_{fs} - \frac{3\mu_l}{h}\vec{V}_l + \dot{q}_s \tag{9}$$

$$\vec{D}_v = \frac{\partial}{\partial s}\int_0^h v_l^2 dy \tag{10}$$

$$P_L = P_{gas} + P_h + P_\sigma \tag{11}$$

$$P_h = -\rho h(\vec{n}.\vec{g}) \tag{12}$$

$$P_\sigma = -\sigma\nabla_s.(\nabla_s h) \tag{13}$$

where, $\rho_l$ depicts the film density, $h$ signifies the height of the film, $V_l$ represents the average film velocity and $\dot{m}_s$ indicates mass source per unit wall area resulting from particle deposition, film stripping, film separation, and phase change. $D_v$ is the differential advection term and is calculated using the quadratic film velocity. $P_L$ designates the film pressure, $g_\tau$ the gravity component, $\tau_{fs}$ represents the shear stress at the liquid-film interface, $\mu_l$ symbolize the viscosity, $\dot{q}_s$ denotes the momentum source, $\sigma$ reflects the surface tension, $P_\sigma$ indicates the pressure contribution due to the surface tension, $P_h$ corresponds to the component of gravitational pressure acting perpendicular to the wall, and $n$ represents the normal vector to

the wall surface. Furthermore, the wetting parameter of the wall is defined by the contact angle, which is 50°. This reflects a moderately hydrophilic surface, corresponding to the physiological circumstances of the human airway lining, which is generally coated with a thin mucus layer. A contact angle of 50° shows that the wall supports partial wetting, which is suitable for simulating particle-wall interactions, especially in simulations involving droplet or particle deposition on realistic airway surfaces. Table I lists the parameters used in computational simulation.

**TABLE I.** Values of simulation parameters.

| Simulation parameters | Value |
|---|---|
| Air density (kg/m$^3$) | 1.225 |
| Air dynamic viscosity (kg/m-s) | $1.7894\times 10^{-5}$ |
| Drug solution density (kg/m$^3$) | 1100 |
| Particle diameter (μm) | 1 to10 |

### H. Computational approach

A flowchart (Fig. 5) depicts the process of setting and solving a coupled DPM-EWF simulation in ANSYS Fluent 2023. The main steps involved are as follows:

First, the CT scan geometry is smoothed, and artifacts are removed using Meshmixer software developed by Autodesk® to ensure a clean and accurate representation of the airway structure. The computational domain is then imported into ICEM CFD in .stl file format to create a high-quality computational grid. After creating the mesh, the .msh file is imported into ANSYS Fluent, where the boundary conditions and fluid flow properties are employed and configured. Following that, initial conditions and particle properties such as diameter, density, and discrete phase settings are given, and a finite volume mesh is constructed for the computational domain. The mesh must be sufficiently refined to resolve particle dynamics and capture critical flow features. Once the initial settings have been established, a suitable turbulence model is chosen depending on the flow parameters. The governing equations for fluid flow (Eqs. 1-4), particle motion (Eqs. 5-7), and thin film dynamics (Eqs. 8-13) in the coupled DPM-EWF model are then numerically solved, taking into account appropriate boundary conditions for both the fluid and particle phases. Before initiating the primary flow study, the complete computational setup is thoroughly tested to ensure adequate grid quality. This procedure includes evaluating the results against experimental and computational benchmarks. Section I contains more

information about the grid independence study and validation techniques. The entire computational investigation was performed on a Dual AMD Genoa 9th series high-performance computing (HPC) processor (128 cores) with 1 TB RAM. The overall computing time to simulate the process for one model is around 74 hours.

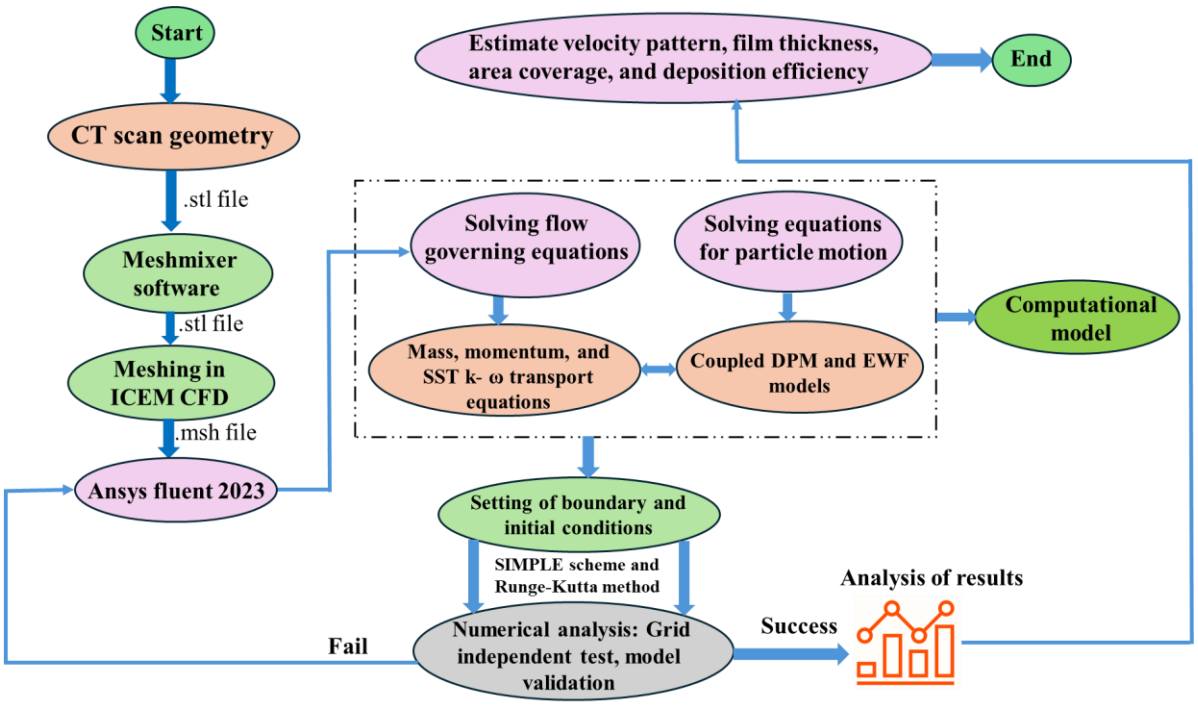


**FIG. 5.** The flowchart of inhaler-based liquid drug particle delivery simulations in a CT-scan-based lung model. The procedure starts with the geometry construction and meshing to coupled airflow-particle modeling with DPM and EWF methods, followed by validation and performance evaluation using ANSYS Fluent 2023 software.

### I. Grid dependency test and model validation

The computational grid (Fig. 6) is generated in ICEM CFD, which consists of unstructured elements with 10 layers of near-wall prism to adequately capture flow dynamics near the boundary more precisely, as seen in Fig. 6(a). A grid dependence test was performed to ensure the mesh density was sufficient to achieve converged results. The meshing procedure employs robust octree and quick Delaunay techniques to improve mesh quality and computational performance. The mesh dependency study included three meshes with element counts ranging from 3 million (3M) to 9M (Fig. 7). The analysis of velocity magnitude fluctuations along the two locations of the human lung revealed negligible changes (0.027%) when the mesh density was increased from 6 to 9M elements. As a result, the current study used a mesh density of 6M elements for the rest of the results. A rigorous validation of the current computational model

against the standard experimental (Kim and Fisher [54]) and numerical (Kim *et al.* [43]) results was performed previously and can be seen from Verma *et al.*[14] Moreover, the computational geometry is validated by those of Bhardwaj *et al.*,[16] showing good agreement.

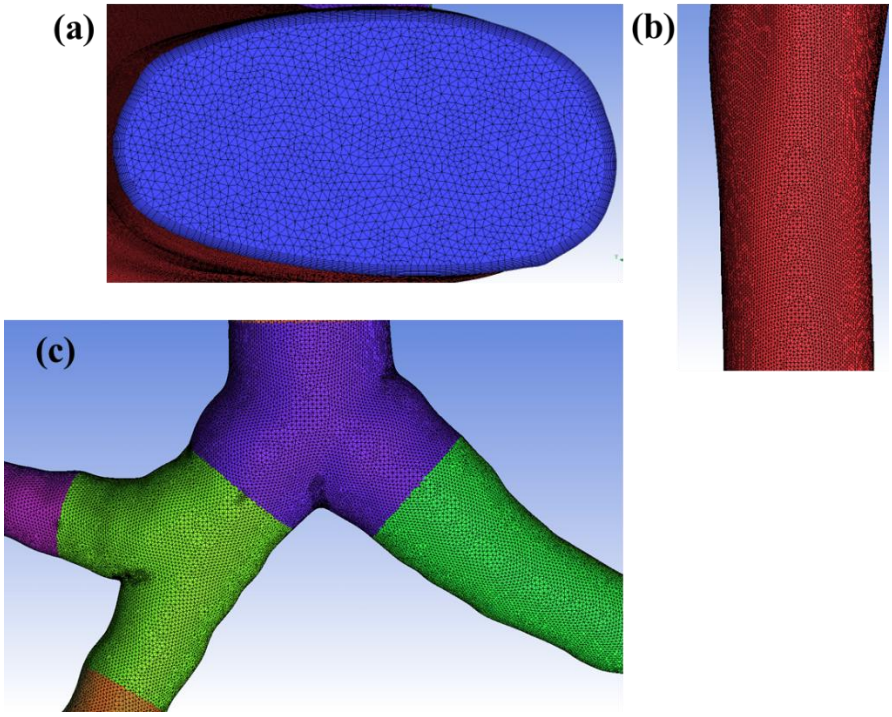


**FIG. 6.** Schematic representation of meshing strategy for a complex, realistic geometry of respiratory airways. The current representations show unstructured tetrahedral grid distributions with 10 inflation layers along the airway wall. The fine mesh ensures accurate resolution of flow characteristics, while boundary refinement near the walls improves deposition predictions. The figures represent the (a) inlet section, (b) tracheal region, and (c) bifurcating airways.

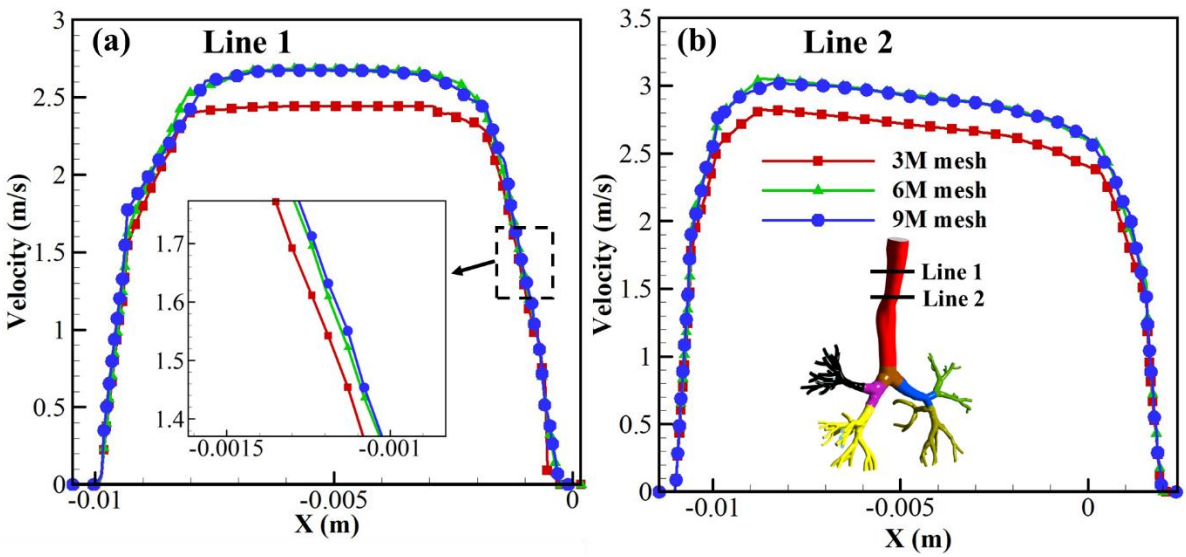

**FIG. 7.** Grid independence test compares velocity distributions at different mesh resolutions along (a) line 1 and (b) line 2. The results demonstrate negligible changes in velocity profile between 6M and 9M meshes. Thus, the rest of the simulations are performed with 6M mesh.

## III. RESULTS AND DISCUSSION

This study examines the deposition efficiency of drug particles under three distinct breathing conditions: ideal, healthy, and diseased (COPD). The particle sizes ranging from 1-10 μm[7, 52] are investigated, assuming a perfectly spherical shape throughout their transport. This section analyzes airflow dynamics and particle behavior inside the human respiratory airways.

### A. Airflow dynamics

Figure 8(a) depicts the velocity magnitude and flow streamlines at various transverse cross-sections across several lobes, including the trachea. These planes extend from the trachea and cover various levels of branches and bifurcations within the left and right lungs. The exact location of the streamwise tracheal plane (plane-A) and the cross-section planes (B to D) are shown in Fig. 3(b). The contours show velocity distribution and flow streamlines for three different breathing rates: ideal, healthy, and COPD. The peak inlet velocity for an ideal, healthy, and COPD case is around 2.1, 4.9, and 10.1 m/s, respectively. It has been observed that even minimal geometrical deflections can modify the streamlines' uniformity, resulting in the formation of secondary vortices. This can be seen in plane B, where a small vortex forms (more visible in the COPD case) at the upper side of the plane as a result of deflection caused by the asymmetrical bulging of the tracheal cross-sections. Secondary vortices are also detected further downstream due to abrupt changes in the flow path, irregular bifurcations, and various deflections in the airway geometry. The flow divides into two parts at the first bifurcation, but because the left main stem bronchus is slightly narrower than the right, the flow accelerates accordingly. This is marked on planes C (left) and D (right). Although the geometry remains constant for all three cases, COPD patients frequently inhale more forcefully due to greater airway resistance in real-life situations, resulting in a higher peak inspiratory flow rate (PIFR). The high-velocity flow in the simulation mimics the real-world scenario in which COPD patients try to compensate for diminished lung efficiency by breathing faster and harder. The finding indicates that, even in an anatomically normal airway, changing breathing profiles can considerably impact airflow behavior and potentially affect particle deposition, oxygen transport efficiency, and overall pulmonary function.

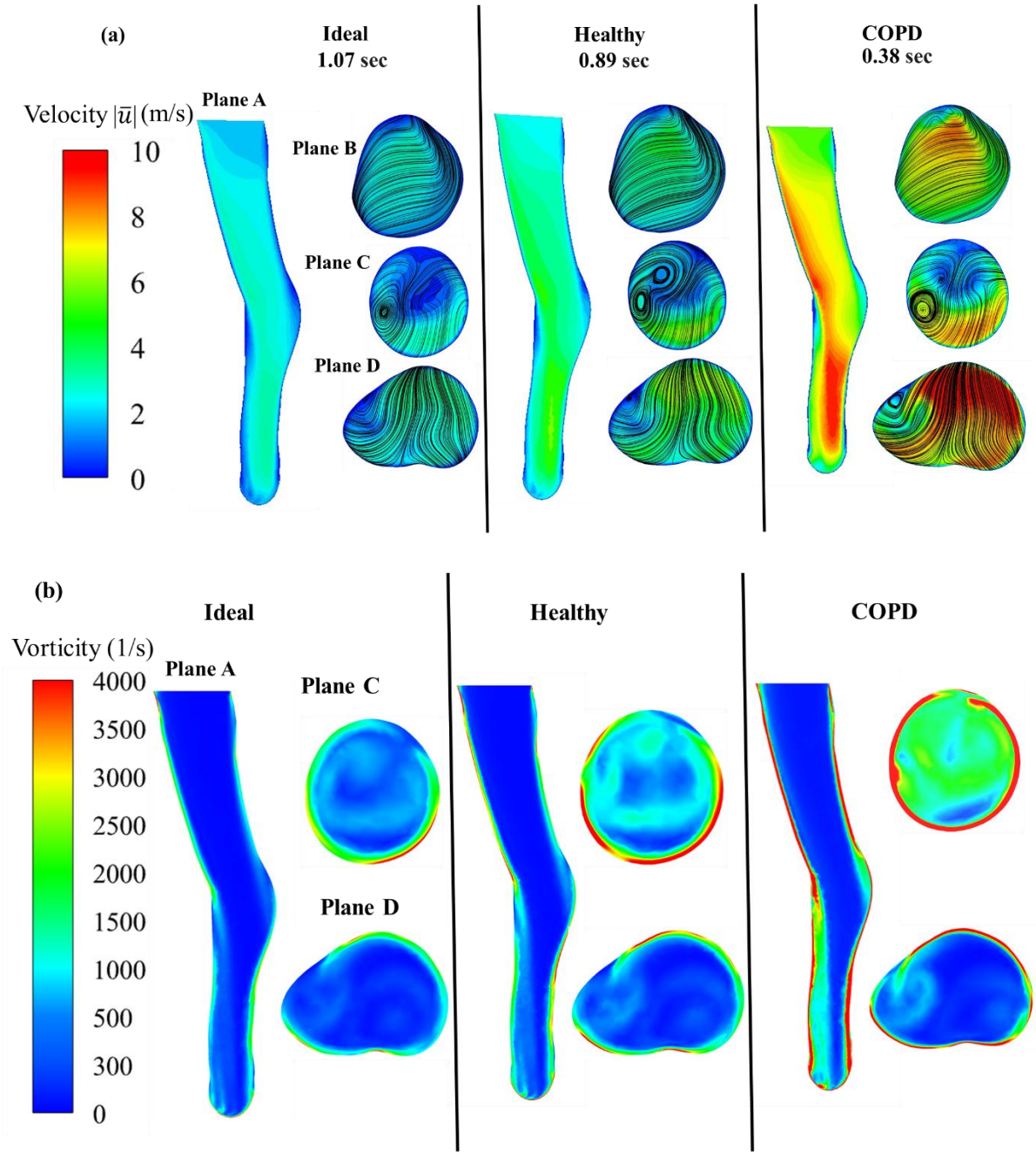


**FIG. 8.** Plots representing (a) streamlines with velocity and (b) vorticity magnitude contours at different cut-planes of the human airway. The contours are extracted at the PIFR of all three ideal, healthy, and COPD breathing profiles. The exact locations of cut-planes A to D are depicted in Fig. 3(b).

Figure 8(b) shows the contours of vorticity magnitude distributions for the ideal, healthy, and COPD breathing instances along the same locations shown in Fig. 8(a). The comparison of the change in vorticity magnitudes highlights the dominating complex rotational flow field of the COPD case compared to the other two. Vorticity is maximum at the outer walls rather than at the center due to the presence of strong velocity gradients and shear layers (Fig. 8b), which

resembles with Bhardwaj *et al.* [16] As can be seen, the maximum vorticity contrasted from 2400 $s^{-1}$ (ideal breathing) to 4000 $s^{-1}$ for the COPD case. In general, plane C has higher vorticity than plane D in all three cases. The COPD breathing depicts the highest vorticity (~4000 $s^{-1}$ in Plane C, ~2500 $s^{-1}$ in Plane D), followed by healthy (3500 $s^{-1}$ in Plane C, ~2500 $s^{-1}$ in Plane D), and then the ideal breathing (~3000 $s^{-1}$ in Plane C, ~2000 $s^{-1}$ in Plane D). The no-slip boundary condition and high shear near the wall cause vorticity gradients towards the center locations. At airway bifurcations, flow redirection causes secondary motions and swirling structures (such as Dean vortices), contributing to increased vorticity near the boundaries. In conditions such as COPD, the turbulent fluctuations become more prominent, and the high shear leads to the maximum turbulent kinetic energy values of 0.4 $m^2/s^2$ compared to ideal and healthy values of 0.007 and 0.015 $m^2/s^2$, respectively. Furthermore, recirculating flow zones near bifurcations produce additional rotating effects, increasing vorticity in these areas. In contrast, the center portion of the airway has a more stable and uniform flow with little velocity fluctuations, resulting in less vorticity. The combination of velocity gradients, boundary layer effects, turbulence, and secondary flow structures results in maximum vorticity near the outer walls.

**B. Deposition and escape pattern of the particle**

Deposition efficiency is expressed as the ratio of particles trapped (absorbed) on the airway walls to particles entering the computational domain through the inlet. It is represented by $\eta_f$, and can be expressed as,

$$\eta_f(\%) = \frac{Number\ of\ particles\ trapped\ on\ the\ airway\ walls}{Number\ of\ particles\ released\ from\ the\ inlet\ of\ the\ computational\ domain} * 100 \qquad (14)$$

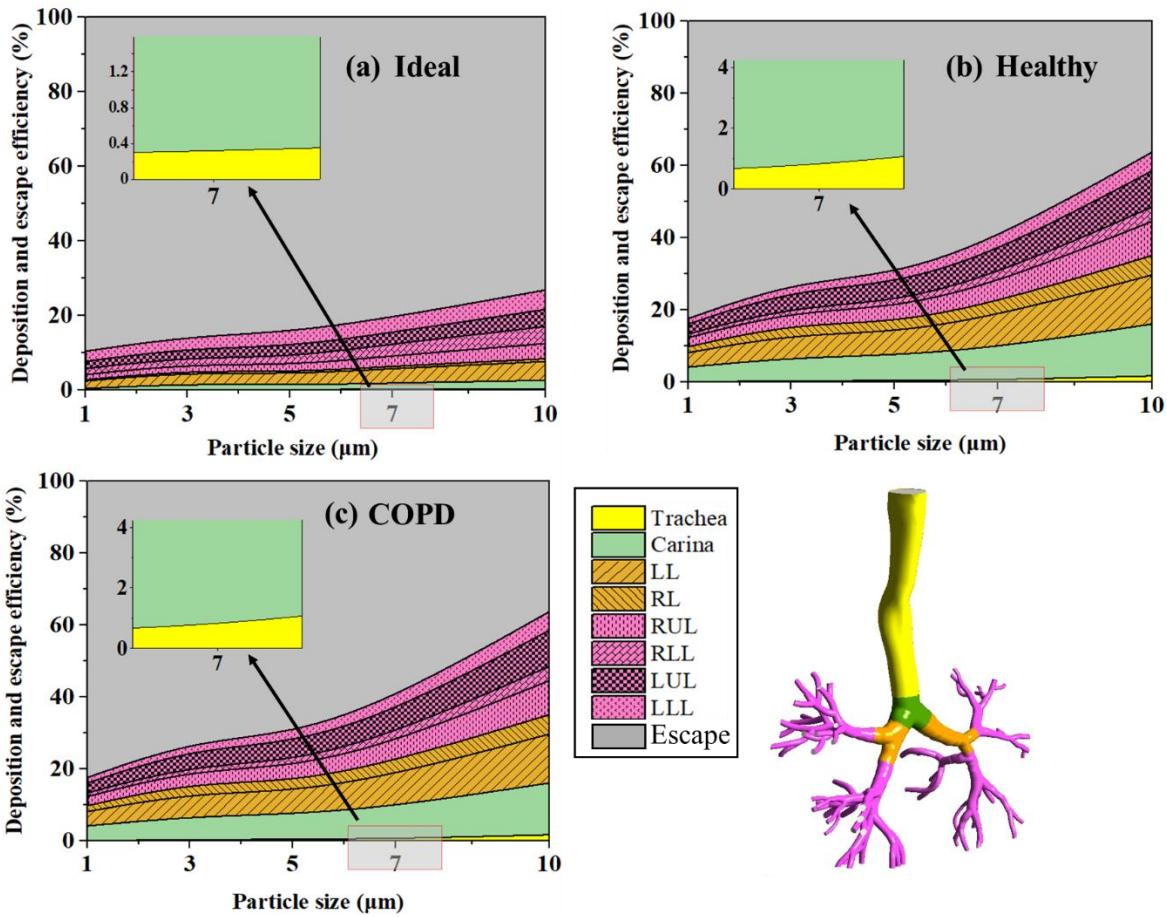


**FIG. 9.** Regime maps showing the deposition efficiencies of inhaled particles across different lung regions and final escape percentage (grey color) from the entire domain till G7. Three distinct maps represent (a) ideal, (b) healthy, and (c) COPD breathing conditions. The deposition patterns are grouped based on different colored lung regions, as illustrated in the right-last image.

Figure 9 depicts the regime map for the deposition and escape efficiency of particles of varying diameters under ideal, healthy, and COPD breathing conditions. The Figure indicates that 10 μm particles have the highest deposition, and 1 μm particles have the least deposition throughout the domain, regardless of breathing rate. This is primarily because inertial impaction becomes less effective as particle diameter decreases. A similar trend has also been reported in a previous study.[55] In ideal and healthy cases, the LLL bronchus and LL exhibit the highest deposition rate for most particle sizes, while the carina, RL, and trachea have the lowest. However, in the case of COPD, the carina has the highest deposition rate, followed by the left and right bronchi. Similar to the particulate diameter, it has been observed that the increase in inhalation rate also monotonically increases the deposition efficiency and subsequently reduces the escape rate. This behavior can be explained by inertial impaction,

which occurs when particles with high inertia are unable to follow the curved flow streamlines, especially at bifurcations or sharp turns in the airway. Changes in flow direction amplify this effect, causing larger particles to deviate from the airflow and impact the airway walls. Consequently, most of the large particles deposit in the upper airway generations, and penetrations to the deeper regions of the lungs are reduced. Smaller particles (1-3 μm) are deposited primarily through diffusion, resulting in a consistent distribution throughout lobes. As particle size exceeds 5 μm, inertial impaction becomes the primary mechanism, resulting in a more distinct variation in deposition between upper and lower lobes.[56] In the case of COPD, intake becomes more forceful and less effective as the airflow velocity changes abruptly, resulting in higher inertial impaction at bifurcations, particularly along the carina (first bifurcation). This limits the deep lung penetration in COPD cases, i.e., fewer particles reach the lower lobes. Moreover, the other complex dynamics, such as air trapping or the formation of local air pockets, make upper airway deposition more prominent in COPD cases.

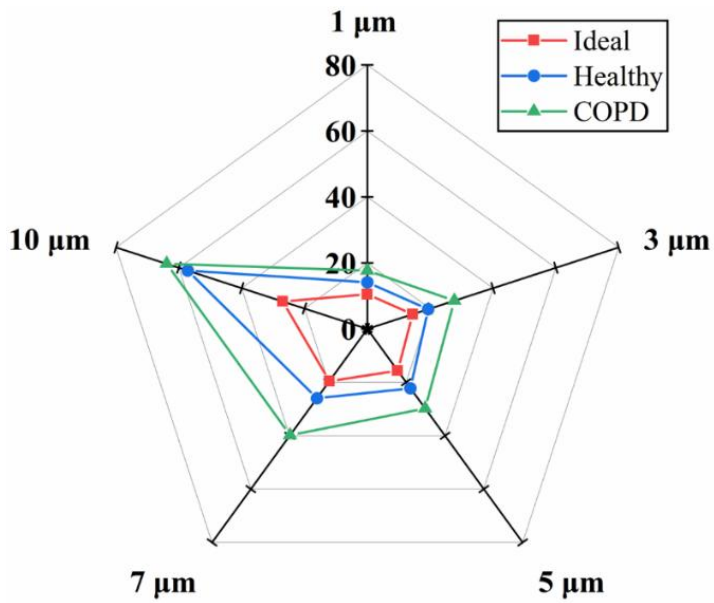


**FIG. 10.** Total deposition efficiency across distinct particles for ideal, healthy, and COPD, highlighting the influence of breathing conditions on deposition behavior for each particle size.

Figure 10 presents a comparative analysis of the total deposition efficiency of inhaled particles, sized between 1 and 10 μm, across the different breathing profiles, namely the ideal, healthy, and COPD cases. As explained earlier, the deposition efficiency of the smaller particles (1-3 μm) is relatively low for all three cases due to their high diffusivity and lower inertia. However, due to disturbed airflow patterns and high velocity, the deposition is still relatively higher in COPD cases (≈ 22.69%) compared to healthy (≈ 16.76%) and ideal (≈ 12.45%) breathing. For

medium-sized particles (5-7 μm), deposition efficiency of the COPD case starts dominating (nearly 34.77% ) compared to healthy and ideal breathing by roughly 22.69% and 17.57%, respectively. This rise in deposition efficiency can be attributed to a combination of inertial impaction and altered flow characteristics in COPD. For larger particles (10 μm), there is a significant difference in deposition efficiencies amongst the breathing profiles. It reaches up to approximately 1.2 and 2.37 times higher for COPD cases compared to healthy and ideal breathing, respectively. Clearly, this trend is dominated by inertial impaction, where gravitational settling is also essential. Conclusively, the short breathing span, formation of local air pockets, higher inertial impaction, and gravitational settling lead to less penetration of the liquid particles in COPD cases.

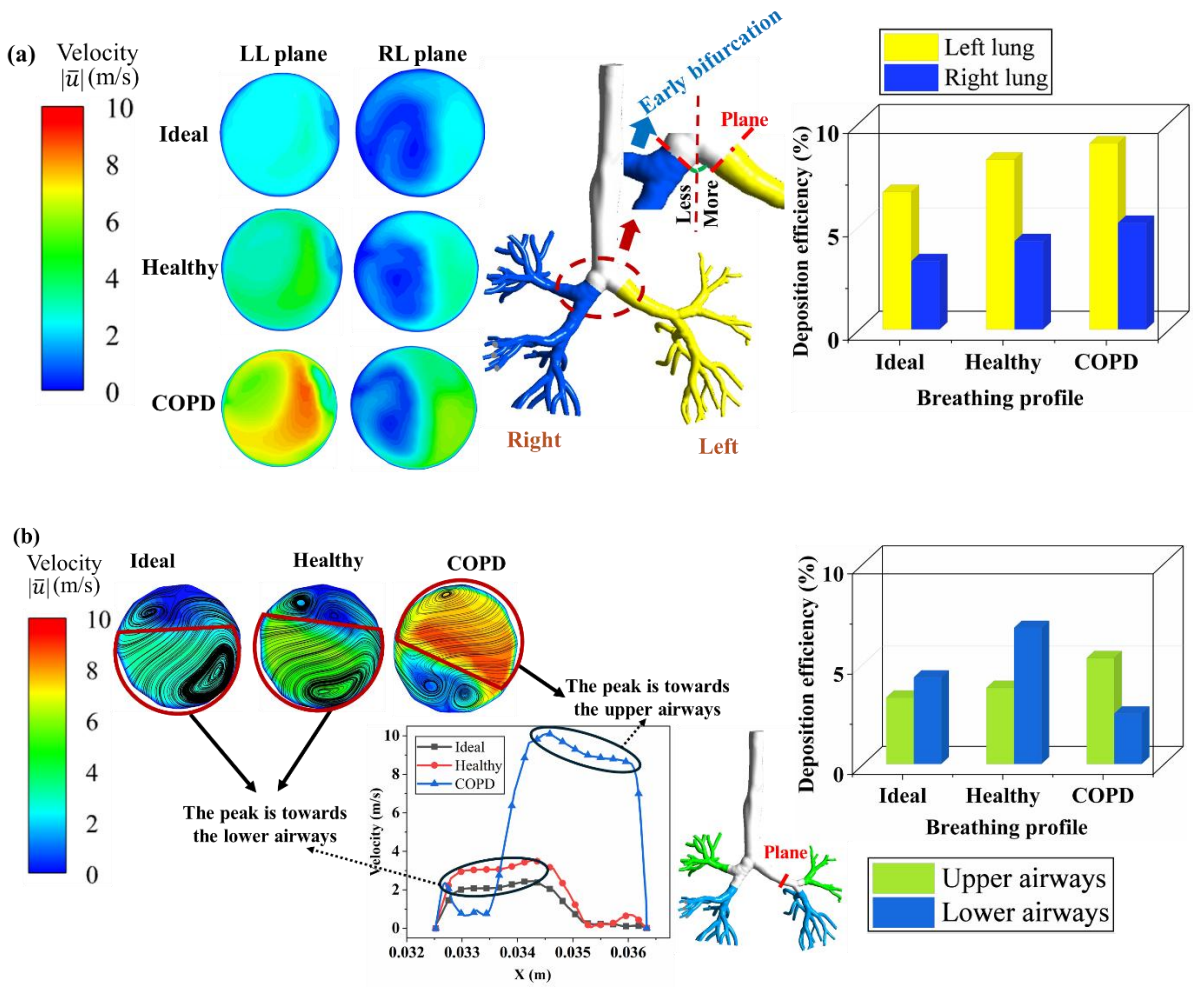


**FIG. 11.** Comparison of particle deposition efficiency in various lung regions for 1 μm particle size. (a) Particle deposition asymmetry between left and right lungs (right), which potentially arises because of the early bifurcation at the right lung (middle) and differences in average velocity magnitude (left) as a result of it and (b) Deposition efficiency contrasts between the

upper and lower lung lobes (right) that arise because of the preferential asymmetries of velocity magnitudes, highlighted using the contour (left) and line (middle) plots.

Figure 11(a) shows that the left lung consistently has a higher deposition efficiency (roughly two times) than the right lung for all three cases of breathing. In an ideal breathing situation, the left lung has approximately 6.64% deposition efficiency, whereas the right lung has around 3.3%. In healthy breathing, deposition in the left lung increases significantly to about 8.21%, while the right lung remains below 4.5%. Although deposition efficiency in the left lung increases marginally in COPD patients (8.99%) compared to healthy individuals, it remains higher than in the right lung (5.15%). The primary reason behind the deposition bias is a considerable disparity in airflow distribution between the two lungs. Specifically, the average velocity magnitude in the right lung is around 38% lower than in the left. This difference in velocity magnitude is because of an early bifurcation [middle image in Fig. 11(a)] along the right bronchus in the airway geometry. This leads to flow stagnation immediately after the first bifurcation and directs a greater proportion of the flow to the left bronchus. Moreover, an asymmetry in the bifurcation angle at the carina also plays a decisive role in the preferential biases of the airflow rate. As a result, fewer particles enter the right lung, whereas increased velocity toward the left lung encourages more particle transport and deposition in that region.

Figure 11(b) highlights the preferential biases in deposition efficiency between the upper and lower lung branching. As shown in the bar plot of Fig. 11(b), the deposition efficiency in the lower airways is higher than the upper airways for both ideal and healthy breathing profiles. However, this trend is completely opposite for the COPD breathing profile. Here, the upper airways display higher deposition (~5.28%) than the lower airways (~2.52%).

The complex airflow dynamics are the fundamental reason behind this preferential asymmetry in deposition efficiency. It has been known and widely established that every airway branching introduces an asymmetry in the velocity distributions.[14, 57] However, in the current situation, this asymmetry in the flow velocity is tweaked in such a way that forced and shortened breathing of COPD leads to a shifting of the velocity peak to the upper side of the airway [left images of Fig. 11(b)]. As a result, more particles are directed towards the upper airway branches. Meanwhile, in both ideal and healthy breathing circumstances, peak velocity is predominantly centered in the lower portion of the airway. This directed momentum drives more particles into the lower airway branches, increasing deposition in those areas. The overall understanding of deposition preference suggests that COPD has different deposition profiles

than normal and idealistic breathing, on which most inhalers are usually designed. Therefore, a patient-specific inhaler-based drug delivery demands special attention to achieve therapeutic outcomes.

Figure 12 depicts a symbolic representation of particle distributions across airway generations. The 1 μm particles scatter more evenly throughout the lung regions than the 5 and 10 μm particles. Smaller particles have lower inertial impaction, allowing them to closely follow fluid streamlines and lessen their chances of colliding with airway walls. As a result, these particles can escape the computational domain and travel into the deeper lungs. Larger liquid particles, on the other hand, are more likely to collide with the airway wall, resulting in more deposition in targeted lung sites.

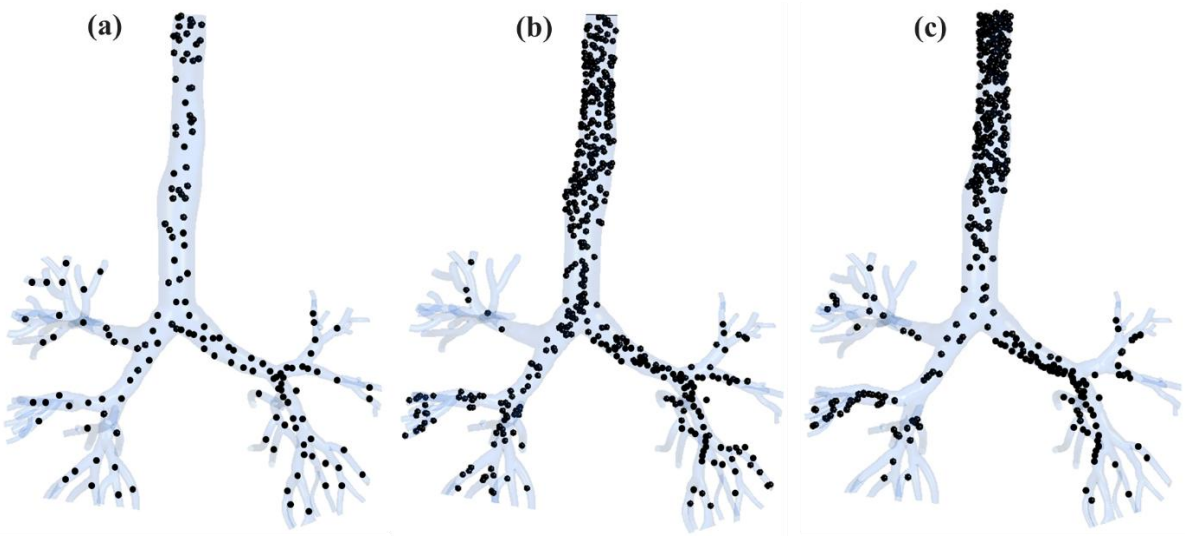


**FIG. 12.** Symbolic representations of spatial particle distribution to highlight the effect of inertial impaction by the (a) 1 μm, (b) 5 μm, and (c) 10 μm particle sizes under healthy breathing conditions.

**C. Film thickness**

The film thickness is the height of the thin liquid layer formed on the airway walls by the deposition and coalescence of tiny droplets. This deposition, combined with existing liquid layers, forms a thin coating. The variation in film thickness depends on different factors, such as the particle shape and size, airway geometry, breathing pattern, and inherent flow dynamics. Figs. 13(a) and 13(b) show typical film thickness distributions for the normal breathing profile and 10 μm particle size. The asymmetry in the velocity distributions at different locations of airways is evident in the contour plots of velocity magnitudes (Figure 8a). This asymmetry leads to selective deposition with each generation [Fig. 13(a)]. As can be seen, over 90% of

particles are deposited along the inner segment of the airway walls rather than the outward regions. To justify the role of velocity asymmetry, a plot of velocity variations along the diameter is shown on the right bronchi [Fig. 13(b)]. The asymmetry in deposition is more pronounced for 5-10 μm particles than for smaller ones [Fig. 13(c)].

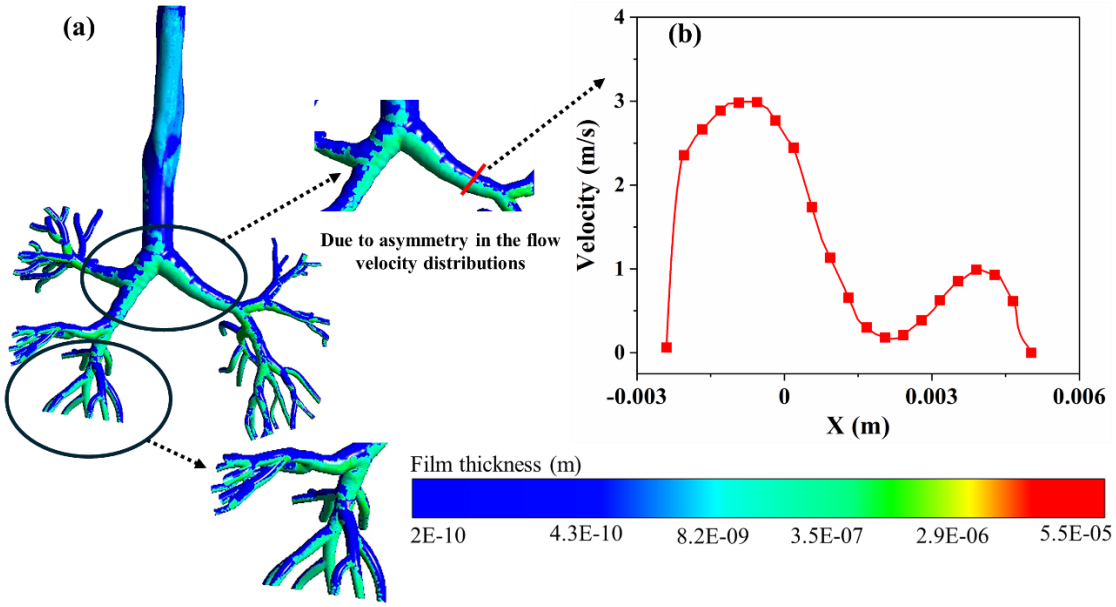


**FIG. 13.** (a) Contour plots of film thickness to represent the particle depositions along inner segments of airways and (b) The asymmetric variations in the velocity magnitudes across the diameter of the airway cause such porous depositions of the film thickness.

The film thickness plots highlight the importance of resolving the post-impaction spread dynamics of the inhaler-based drug delivery mechanism. It captures the precise location of particulate deposition and overall area coverage to give a comprehensive picture of drug delivery efficacy. Generally, the zonal subdivision terminology of airways defined the entire annular wall with 360° rotations as a single zone. As a result, the previously employed pure DPM approach cannot capture the porosity in depositions along any designated airway zone. In contrast, the EWF allows us to capture not only the precise location of depositions, but also the post-striking dynamics, such as the spreads and interactions of initially deposited drugs caused by the shear of the surrounding airflow. Thus, relying on just DPM-based approaches compromises the accuracy of drug delivery predictions.

A similar trend of change in deposition efficiency with the particle size and different breathing patterns is evident in the variation of film thickness comparison shown in Fig. 13(c). However,

the film thickness distribution on these plots suggests that the overall extent of area coverage in each zone has significant porosity. In the case of COPD breathing, film thickness is more prominent in the upper airways compared to both ideal and healthy breathing due to the characteristics of altered airflow dynamics. COPD patients experience increased airway resistance and turbulence, which promote impaction and particle deposition in the upper bronchial region. The constrained airflow reduces particle delivery to the lower airways, producing less film accumulation. This situation significantly impacts drug delivery efficacy because of the complex airflow dynamics that prevent effective deep lung deposition.

Compared to the healthy case, the ideal breathing has the smallest film thickness for all particle sizes. The natural variations in airflow rate, acceleration, and turbulence in healthy breathing enhance inertial impaction and convective transport of particles. In contrast, the ideal breathing profile shows a smooth, idealized inhalation cycle without the strong acceleration peaks that are found in normal human breathing patterns. The absence of considerable turbulence (turbulent kinetic energy $\approx 0.007\ m^2/s^2$ for the ideal and $0.015\ m^2/s^2$ for the healthy) minimizes impaction, resulting in less deposition in the airway. Instead, the particles diffuse uniformly throughout the airways, resulting in a thinner film layer in ideal breathing. Medically, sinusoidal breathing does not entirely resemble physiological conditions, but it does provide a simple model for demonstrating how controlled airflow reduces impaction.

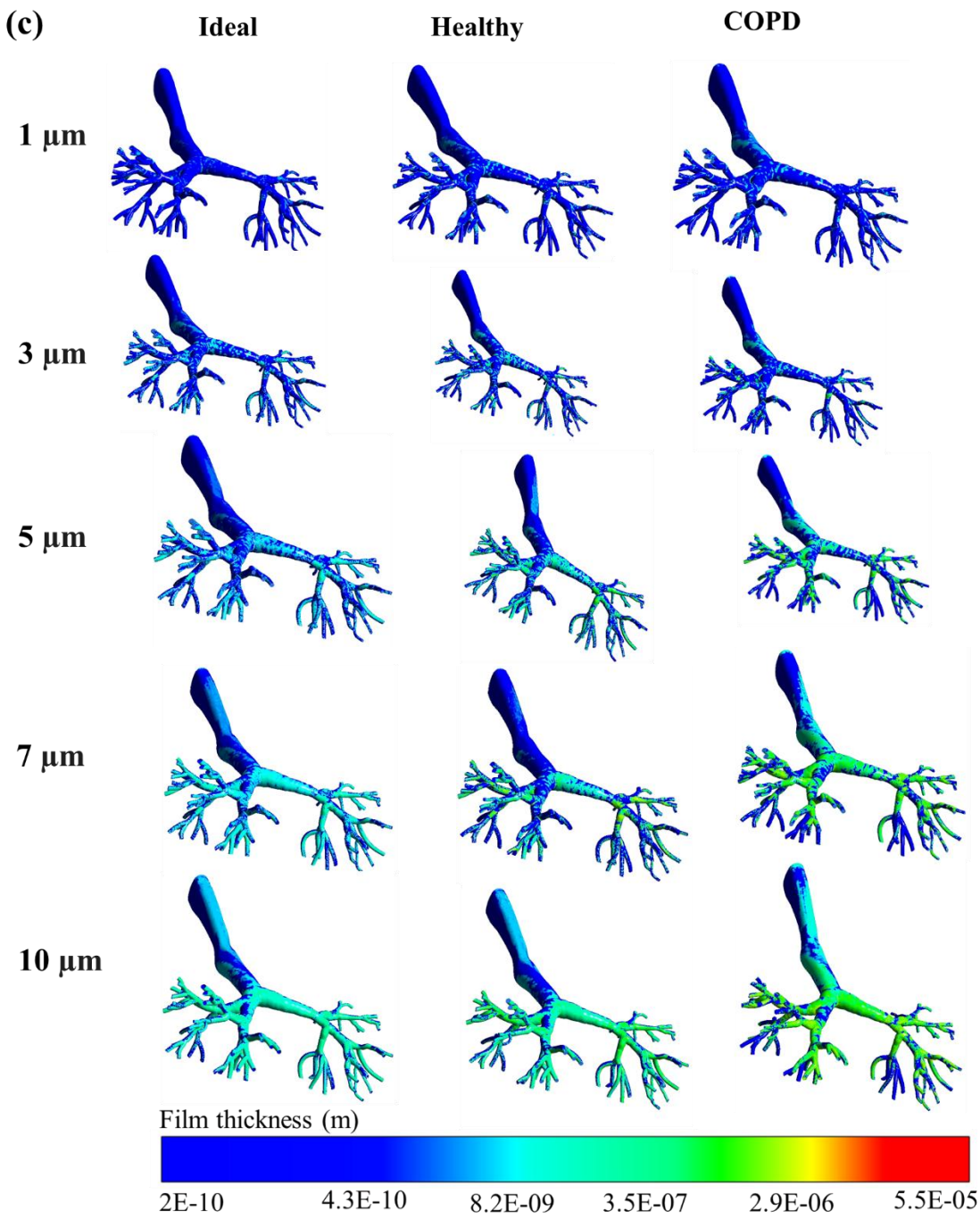


**FIG. 13(c).** Comparison in film thickness variations for the particle sizes ranging from 1 to 10 µm under all three inhalation cases. Higher thickness appears for the larger particle size due to inertial impaction, whereas the forceful breathing of the COPD patient leads to a relatively higher film thickness.

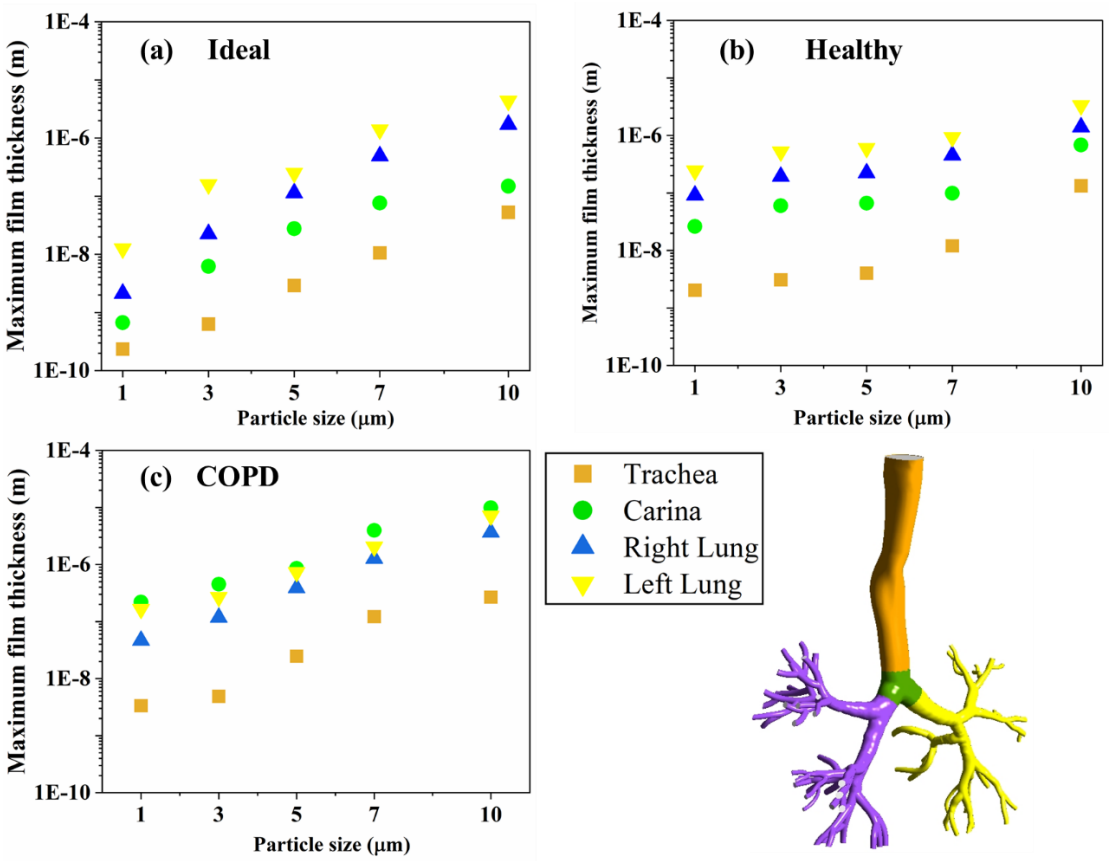


**FIG. 14.** Comparison of film thickness deposition for various particle sizes (1-10 μm) in the different airway segments under (a) ideal, (b) healthy, and (c) COPD conditions. The Y-axis displays maximum film thickness variations on a logarithmic scale. The color tagging of the symbols is linked with the equivalent zone for better understanding (bottom right image).

Figure 14 compares how the film thickness at different locations changes with the change in particle size for all three breathing cases. The distribution of maximum film thickness at different zones follows a similar trend in both the ideal and healthy breathing situations [Figs. 14(a) and 14(b)]. The left lung consistently has the maximum film thickness, which is nearly 2.63 times greater in the ideal case and roughly 5.94 times greater in the healthy case than the right lung thickness for all the particle sizes in an averaged sense. However, the film thickness in the trachea is almost negligible and significantly lower in the carina (15 times for healthy and 23.7 times for ideal breathings) compared to the maximum left lung depositions in the healthy and ideal breathing situations. In contrast, the COPD instance shows the completely opposite trend for maximum film distributions [Fig. 14(c)]. Unlike the other two, the maximum film thicknesses are observed in the carina region rather than the left or right lungs, which is the first bifurcation at the trachea. The maximum film thickness is roughly 1.48 times lower

for the left and 2.83 times lower in the right lung compared to the maximum carina region. Moreover, it has been observed that the general distributions of maximum film thickness in almost all the regions for COPD cases are nearly an order of magnitude higher ($10^{-6}$ m) than in ideal and healthy breathing situations. The shortened and forceful breathing in COPD cases introduced a contrasting difference in the distribution and overall deposition of maximum film thickness. This suggests that the change in the breathing pattern significantly influences the inhalation airflow dynamics inside the airways. This leads to the formation of flow recirculation, secondary vortices, higher turbulent intensity, and increased airway resistance.

**D. Film area coverage**

The film area coverage (Fig. 15) is the percentage of a surface covered by a liquid film after deposition, expressed as the wet area fraction. In other words, it is the proportion of the entire surface area covered in each individual lobe by a liquid film generated by drug solutions upon impact. This parameter is critical in inhalation drug administration since it influences how well the medication spreads along the airway lining. Smaller particles are less impacted by inertia and can remain suspended in the airflow for longer periods, minimizing their tendency to settle and deposit on the airway walls. The stack plots in Fig. 16 illustrate the area coverage (%) of thin drug film coatings on various airway regions for different particle sizes (1-10 μm). The area coverage plot is critical in understanding the spatial pattern of particle deposition throughout the individual regions of the respiratory tract. Here, capturing area coverage is made possible by coupling the thin film approximation (EWF) approach with the DPM-based particle tracking. In contrast to deposition efficiency, which measures the total fraction of inhaled particles that deposit anywhere in the lungs, area coverage focuses on where those particles settle and what fraction of the airway surface area is covered.

In Fig. 15, the four major regions mentioned initially, namely the trachea, carina, right, and left lungs, are further segmented into eight different zones to predict the deposition behavior more precisely. Specifically, the right and left lung regions are further split into the upper (RUL, LUL) and lower (RLL, LLL) lobes. This segmentation enables us to understand the greater resolution of spread patterns and helps identify region-specific accumulation. Such denotations are helpful in the clinical assessments of targeted drug delivery. Each colored segment within a column of the stacked plots denotes the percentage of area coverage against the total area of that particular zone. For example, the floating top position of the orange color legend signifies that the LLL has the highest area coverage percentage, which is nearly 55.2% for 10 μm particle

sizes in ideal breathing [Fig. 15(a)]. In contrast, the carina region has the highest area coverage for the COPD scenario, around 71.51% for 10 µm particles. Thus, the cyan color legend has a floating top position. Specifically, for ideal and healthy breathing, the maximum coverage is at the LLL region of the lungs, which is 55.2% and 63.48%, respectively [Fig. 15(a) and 15(b)]. However, the maximum coverage for COPD is in the carina region, which is 71.51% [Fig. 15(c)]. This region-wise specific coverage spread is impossible to calculate when only the DPM-based approach is used in drug delivery investigations.

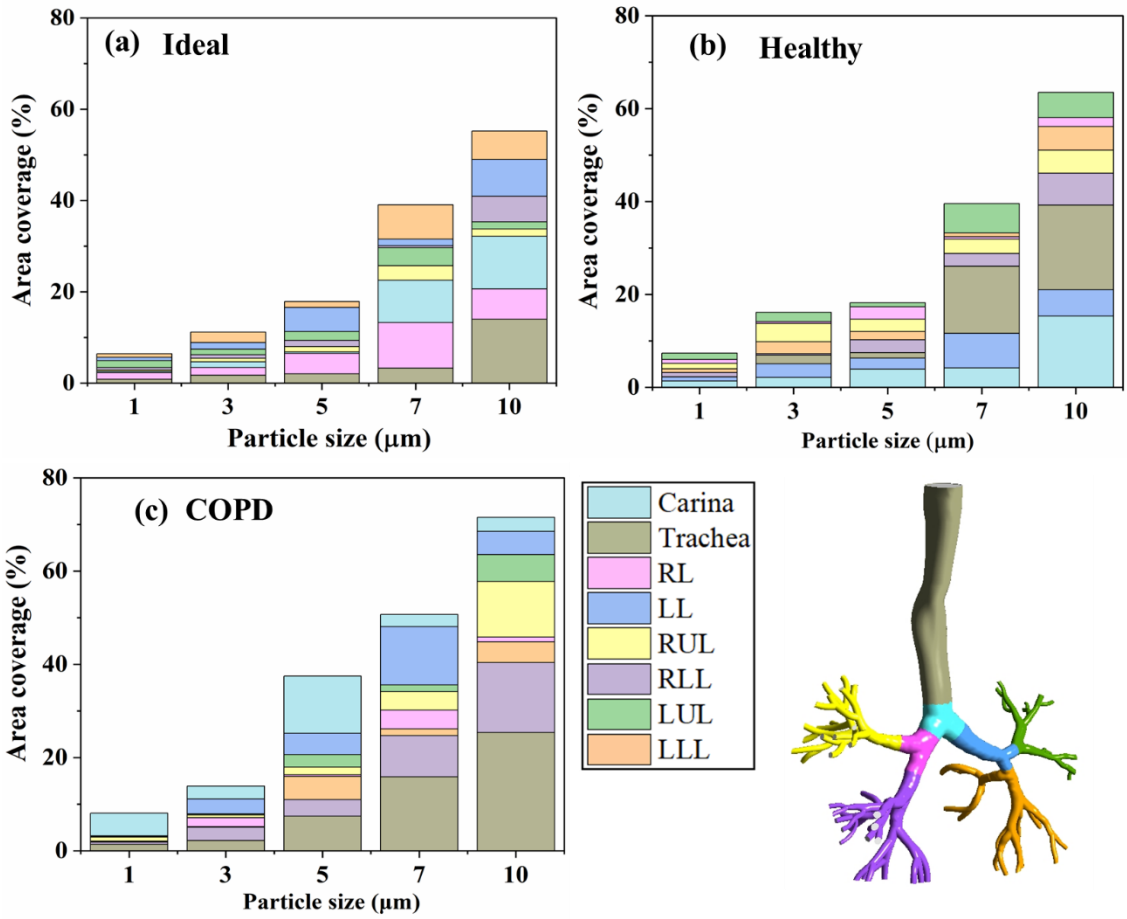


**FIG. 15.** The stack plots show the comparison of area coverage (%) obtained from the particle sizes ranging from 1-10 µm for the (a) ideal, (b) healthy, and (c) COPD cases. The exact value of area coverage (%) on each individual color zone can be interpreted by its absolute value from the zero reference point rather than the visible extent of color shedding.

## V. LIMITATIONS OF THE STUDY

Several limitations of the current investigation should be acknowledged, especially when interpreting the results in the context of inhalation therapy. The study considers only the

inhalation phase of breathing. Although simulating the full respiratory cycle (inhalation and exhalation) would yield a more comprehensive understanding of particle behavior, the current model is limited because there is no reliable data to model particle retentions at lower lung generations.[58, 59] Moreover, there is no defined mechanism to account for particles that might remain airborne and re-enter the modeled domain during exhalation. All these factors make it difficult to simulate exhalation-phase deposition accurately. Another simplification involves the assumption of rigid airway walls. In reality, the airway tissues exhibit some degree of elasticity, which can influence airflow and deposition patterns. Furthermore, the current work has not considered the effect of the viscoelastic mucus layer in the respiratory tract model. Despite these limitations, the simulation results for airflow behavior and particle deposition align well with findings in existing literature, lending confidence to the overall validity of the study.

## VI. SUMMARY AND CONCLUSIONS

This study utilizes a CT scan-based realistic human lung model, extending up to the seventh generation from the trachea (G0-G7), to analyze the efficacy of particle depositions. A numerical investigation examines the effects of five distinct particle sizes between 1-10 µm under three breathing condition rates (ideal, healthy, and COPD). Additionally, the coupled DPM and EWF model is employed to evaluate the deposition behavior of particle interactions within the respiratory airways.

The key findings of the current research work are outlined below:

- The velocity and vorticity distribution contours suggest the presence of a highly disturbed, rotational flow field because of the short and forceful breathing of a COPD patient compared to the ideal and healthy person's breathing pattern. A variation in maximum vorticity magnitude is 4000 $s^{-1}$ for a COPD patient compared to ideal (3000 $s^{-1}$) and healthy (3500 $s^{-1}$) breathings. Such a disturbed flow field tweaks the deposition dynamics of inhaled drug particles and affects their distributions.
- Larger liquid particles and higher inhalation rates result in an increased impaction and reduce the particles' ability to follow airflow streamlines and adjust to directional changes. This leads to a phenomenon known as inertial impaction, which causes higher deposition because of the elevated Stokes number.

- The deposition efficiency has been observed to increase monotonically with the increase in particle size for the cases of all three transient breathings. This pattern varies from 12.45 – 26.96% for ideal breathing, 16.76% – 57.17% for healthy breathing, and 22.69% – 63.89% for the COPD cases in an averaged sense as the particle sizes are increased from 1-10 µm.
- In general, the short and forceful breathings of COPD cause a significantly higher deposition efficiency than the other two cases for all particle sizes. This increase is roughly 2.05 and 1.28 times, on average, for the ideal and healthy cases, respectively.
- The complex rotational flow dynamics introduced by the short and forceful breathing of COPD have a significant impact on the region-wise deposition efficacy. COPD breathing shows higher deposition along the upper lung lobes, which otherwise have a contrasting preference for ideal and healthy breathing. Ideal and healthy breathing shows higher deposition along the lower lungs.
- The variation in the maximum film thickness and area coverage follows the patterns of the deposition efficiency parameter. However, as these two parameters grossly account for the effect of post-deposition dynamics, a lot more information related to the precise location of drug spread can be extracted from here. For example, the highest area coverage and maximum film thickness are recorded in COPD breathing along the carina region. This peculiar property of COPD has not been revealed unless the EWF model has been employed with the traditional DPM approach.
- The ideal and the healthy breathing pattern shows the contrastingly different locations of the highest area coverage and maximum film thickness. These values are higher in the left lower lobe (LLL) in place of the carina, as in the case of COPD.
- This study reveals that during impaired breathing, drug penetration into the deep lung is significantly reduced compared to ideal and healthy inhalation. This reduction occurs due to altered airflow dynamics, increased airway resistance, and turbulence, which result in greater deposition in the upper airways and less drug reaching the lower respiratory regions.
- Therefore, advanced inhalers such as spacers, valved holding chambers with pMDIs, vibrating mesh nebulizers, and some breathing exercises such as *pursed-lip breathing* are essential to slow particle velocity, allowing deeper penetration for better treatment. The study emphasizes the need to combine patient-specific geometry with dynamic inhalation patterns to deliver more effective respiratory therapy.

## ACKNOWLEDGEMENTS:

We thank the organization of the "International Conference on Biological Innovation, Technology, Engineering and Sciences (BITES-2024)" of the "NIT Rourkela and NIT Uttarakhand" in "Rourkela, Odisha, India" held over 18–20 December 2024.
The authors are grateful for having the opportunity to use the high-performance computing (HPC) system at the Department of Mechanical Engineering, NIT Rourkela, through the ISRO-funded project "Design of Micro Cryogenic Coolers for Phased Array Receiver" (Project ID: RES-ISTRAC-2022-008). Author Saurabh Bhardwaj acknowledges the Intramural Seed Grant funding (902/R&C/2023-24) from MNNIT Allahabad, Prayagraj.

## AUTHOR DECLARATIONS

### Conflict of Interest

The authors have no conflicts to disclose.

## AUTHOR CONTRIBUTIONS

**Sameer Kumar Verma:** Data curation (equal); Formal analysis (equal); Investigation (equal); Methodology (equal); Software (equal); Validation (equal); Visualization (equal); Writing – original draft (equal). **Saurabh Bhardwaj:** Conceptualization (equal); Formal analysis (equal); Project administration (equal); Supervision (equal); Writing – review & editing (equal). **Kishore Singh Patel:** Conceptualization (equal); Funding acquisition (equal); Project administration (equal); Resources (equal); Software (equal); Supervision (equal); Writing – review & editing (equal). **B. Kiran Naik:** Conceptualization (equal); Funding acquisition (equal); Project administration (equal); Software (equal); Supervision (equal); Writing – review & editing (equal).

## DATA AVAILABILITY

The data that support the findings of this study are available from the corresponding author upon reasonable request.

## REFERENCES


[1]F. J. Kelly and J. C. Fussell, "Air pollution and airway disease," Clin Exp Allergy. 41(8):1059-1071. doi:10.1111/j.1365-2222.2011.03776.x (2011).

[2]M. B. Dolovich, A. Kuttler, T. J. Dimke, and O.S. Usmani, "Biophysical model to predict lung delivery from a dual bronchodilator dry-powder inhaler," Int J Pharm X. 1(May):100018. doi:10.1016/j.ijpx.2019.100018 (2019).

[3]J. Dhanani, J. F. Fraser, H. K. Chan, J. Rello, J. Cohen, and J. A. Roberts, "Fundamentals of aerosol therapy in critical care," Crit Care. 20(1):1-16. doi:10.1186/s13054-016-1448-5 (2016).

[4]S. Christou, T. Chatziathanasiou, S. Angeli, P. Koullapis, F. Stylianou, J. Sznitman, H. H. Guo, and S. C. Kassinoset, "Anatomical variability in the upper tracheobronchial tree: Sex-based differences and implications for personalized inhalation therapies," J Appl Physiol. 130(3):678-707. doi:10.1152/JAPPLPHYSIOL.00144.2020 (2021).

[5]E. Nof, A. A. Schnirman, S. Bhardwaj, H. Sabatan, D. Waisman, O. Hochwald, M. Gruber, L. B. Levin, and J. Sznitman, "Ventilation-induced epithelial injury drives biological onset of lung trauma in vitro and is mitigated with prophylactic anti-inflammatory therapeutics," Bioeng. Transl. Med.7:e10271.doi:10.1002/btm2.10271 (2022).

[6] J. Rissler, M.P. Sjögren, J. Linell, A.L. Hurtig, P. Wollmer, and J. Löndahl, "An experimental study on lung deposition of inhaled 2 μm particles in relation to lung characteristics and deposition models," Part Fibre Toxicol. 20(1):1-14. doi:10.1186/s12989-023-00551-9 (2023).

[7]K. Ahookhosh, S. Yaqoubi, M. Mohammadpourfard, H. Hamishehkar, and H. Aminfar, "Experimental investigation of aerosol deposition through a realistic respiratory airway replica: An evaluation for MDI and DPI performance," Int J Pharm. 566 (May):157-172. doi:10.1016/j.ijpharm.2019.05.058 (2019).

[8]C. Wu, W. Yan, R. Chen, Y. Liu, and G. Li, "Numerical study on targeted delivery of magnetic drug particles in realistic human lung," Powder Technol. 397:116984. doi:10.1016/j.powtec.2021.11.028 (2022).

[9]E. R. Weibel, "Morphometry of the Human Lung," Springer Verlag and Academic Press: New York, doi: 10.1007/978-3-642- 87553-3 (1963).

[10]G. B. Xu, and C. P. Yu, "Effects of age on deposition of inhaled aerosols in the human lung,"

Aerosol Sci Technol. 5(3):349-357. doi:10.1080/02786828608959099 (1986).

[11] J. K. Comer, C. Kleinstreuer, S. Hyun, and C. S. Kim, "Aerosol transport and deposition in sequentially bifurcating airways," J Biomech Eng. 122(2):152-158. doi:10.1115/1.429636 (2000).

[12]M. M. Rahman, M. Zhao, M. S. Islam, K. Dong, and S.C. Saha, "Aging effects on airflow distribution and micron-particle transport and deposition in a human lung using CFD-DPM approach," Adv Powder Technol. 32(10):3506-3516. doi:10.1016/j.apt.2021.08.003 (2021).

[13]M. M. Rahman, M. Zhao, M. S. Islam, K. Dong, and S.C. Saha, "Nanoparticle transport and deposition in a heterogeneous human lung airway tree: An efficient one path model for CFD simulations," Eur J Pharm Sci. 177(July):106279. doi:10.1016/j.ejps.2022.106279 (2022).

[14]S. K. Verma, K. S. Patel, and B. K. Naik, "Coupled Discrete Phase and Eulerian Wall Film Models for Drug Deposition Efficacy Analysis in Human Respiratory Airways," Mol. Pharm. 101-112. doi:10.1021/acs.molpharmaceut.4c00482 (2024).

[15]M. M. Rahman, M. Zhao, M. S. Islam, K. Dong, and S.C. Saha, "A numerical study on sedimentation effect of dust, smoke and traffic particle deposition in a realistic human lung," Int J Multiph Flow. 171 (October):104685. doi:10.1016/j.ijmultiphaseflow.2023.104685 (2023).

[16]S. Bhardwaj, P. Koullapis, S. C. Kassinos, and J. Sznitman, "Fate of inhaled aerosols under the influence of glottal motion in a realistic in silico human tracheobronchial tree model," Eur J Pharm Sci. 173(March). doi:10.1016/j.ejps.2022.106172 (2022).

[17]M. Rahman, M. Zhao, M. S. Islam, K. Dong, and S.C. Saha, "Numerical study of nano and micro pollutant particle transport and deposition in realistic human lung airways," Powder Technol. 402:117364. doi:10.1016/j.powtec.2022.117364 (2022).

[18]J. M. Oakes, S.C. Roth, and S.C. Shadden, "Airflow Simulations in Infant, Child, and Adult Pulmonary Conducting Airways," Ann Biomed Eng. 46(3):498-512. doi:10.1007/s10439-017-1971-9 (2018).

[19]H. B. Mortazavy, H. Mortazavi, F. Aghaei, and S. Kamalipour, "Experimental tracking and numerical mapping of novel coronavirus micro-droplet deposition through nasal inhalation in the human respiratory system," Biomech Model Mechanobiol. 20(3):1087-

1100. doi:10.1007/s10237-021-01434-8 (2021).

[20]M. H. Taheri, O. Pourmehran, M. M. Sarafraz, K. Ahookhosh, A. Farnoud, and X. Cui, "Effect of swirling flow and particle-release pattern on drug delivery to human tracheobronchial airways," Biomech Model Mechanobiol. 20(6):2451-2469. doi:10.1007/s10237-021-01518-5 (2021).

[21]J. Wedel, P. Steinmann, M. Štrakl, M. Hriberšek, Y. Cui, and J. Ravnik, "Anatomy matters: The role of the subject-specific respiratory tract on aerosol deposition — A CFD study," Comput Methods Appl Mech Eng. 401:115372. doi:10.1016/j.cma.2022.115372 (2022).

[22]M. S. Islam, P. Larpruenrudee, A.R. Paul, G. Paul, T. Gemci, Y. Gu, and S. C. Saha, "SARS CoV-2 aerosol: How far it can travel to the lower airways?," Phys Fluids. 33(6). doi:10.1063/5.0053351 (2021).

[23]M. S. Islam, M. M. Rahman, P. Larpruenrudee, A. Arsalanloo, H. M. Beni, M. A. Islam, Y. T. Gu, and E. Sauret, "How microplastics are transported and deposited in realistic upper airways?," Phys Fluids. 35(6). doi:10.1063/5.0150703 (2023).

[24]H. H. Riaz, A. H. Lodhi, A. Munir, M. Zhao, U. Farooq, M. N. M. Qadri, and M. S. Islam, "Breathing in danger: Mapping microplastic migration in the human respiratory system," Phys Fluids. 36(4). doi:10.1063/5.0205303 (2024).

[25]A. Vulović, J. Lamovec, S. Jaćimovski, and N. Filipović, "Transient Numerical Simulation of Airflow Characteristics in the Mouth-Throat 3D Model," Teh Vjesn. 29(5):1507-1513. doi:10.17559/TV-20211123102414 (2022).

[26]C. Atzeni, G. Lesma, G. Dubini, M. Masi, F. Rossi, and E. Bianchi, "Computational fluid dynamic models as tools to predict aerosol distribution in tracheobronchial airways," Sci Rep. 11(1):1-23. doi:10.1038/s41598-020-80241-0 (2021).

[27]J. Zhao, Y. Feng, and C. A. Fromen, "Glottis motion effects on the particle transport and deposition in a subject-specific mouth-to-trachea model: A CFPD study," Comput Biol Med. 116(November 2019):103532. doi:10.1016/j.compbiomed.2019.103532 (2020).

[28]A. V. Kolanjiyil, C. Kleinstreuer, and R. T. Sadikot, "Computationally efficient analysis of particle transport and deposition in a human whole-lung-airway model. Part II: Dry powder inhaler application," Comput Biol Med. 84(May 2016):247-253. doi:10.1016/j.compbiomed.2016.10.025 (2017).

[29]A. R. Lambert, P. T. O'Shaughnessy, M. H. Tawhai, E. A. Hoffman, and C. L. Lin, "Regional

deposition of particles in an image-based airway model: Large-eddy simulation and left-right lung ventilation asymmetry," Aerosol Sci Technol. 45(1):11-25. doi:10.1080/02786826.2010.517578 (2011).

[30]A. Farnoud, H. Tofighian, I. Baumann, G. J. M. Garcia, O. Schmid, E. Gutheil, and M. M. Rashidi, "Large eddy simulations of airflow and particle deposition in pulsating bi-directional nasal drug delivery," Phys Fluids. 32(10). doi:10.1063/5.0024264 (2020).

[31]J. Jedelsky, F. Lizal, and M. Jicha, "Characteristics of turbulent particle transport in human airways under steady and cyclic flows," Int J Heat Fluid Flow. 35:84-92. doi:10.1016/j.ijheatfluidflow.2012.01.003 (2012).

[32]A. R. Paul, F. Khan, A. Jain, and S. C. Saha, "Deposition of smoke particles in human airways with realistic waveform," Atmosphere (Basel). 12(7):1-22. doi:10.3390/atmos12070912 (2021).

[33]A. Naseri, S. Shaghaghian, O. Abouali, and G. Ahmadi, "Numerical investigation of transient transport and deposition of microparticles under unsteady inspiratory flow in human upper airways," Respir Physiol Neurobiol. 244(July):56-72. doi:10.1016/j.resp.2017.06.005 (2017).

[34]E. Makris, M. Pilou, P. Neofytou, S. Tsangaris, and C. Housiadas, "Particle transport and deposition under high-frequency oscillatory ventilation and normal breathing," Aerosol Sci Technol. 48(2):150-162. doi:10.1080/02786826.2013.865831 (2014).

[35]A. Tiwari, A. Jain, A. R. Paul, and S. C. Saha, "Computational evaluation of drug delivery in human respiratory tract under realistic inhalation," Phys Fluids. 33(8). doi:10.1063/5.0053980 (2021).

[36]B. Grgic, A. R. Martin, and W. H. Finlay, "The effect of unsteady flow rate increase on in vitro mouth-throat deposition of inhaled boluses," J Aerosol Sci. 37(10):1222-1233. doi:10.1016/j.jaerosci.2006.01.003 (2006).

[37]W. Hofmann, "Modelling inhaled particle deposition in the human lung-A review," J Aerosol Sci. 42(10):693-724. doi:10.1016/j.jaerosci.2011.05.007 (2011).

[38]J. I. Choi and C. S. Kim, "Mathematical analysis of particle deposition in human lungs: An improved single path transport model," Inhal Toxicol. 19(11):925-939. doi:10.1080/08958370701513014 (2007).

[39]N. D. Khoa, K. Kuga, K. Inthavong, and K. Ito, "Coupled Eulerian Wall Film-Discrete Phase

model for predicting respiratory droplet generation during a coughing event," Phys Fluids. 35(11). doi:10.1063/5.0174014 (2023).

[40]F. Lizal, M. Belka, J. Adam, J. Jedelsky, and M. Jicha, "A method for in vitro regional aerosol deposition measurement in a model of the human tracheobronchial tree by the positron emission tomography," Proc Inst Mech Eng Part H J Eng Med. 229(10):750-757. doi:10.1177/0954411915600005 (2015).

[41]F. Lizal, J. Elcner, P. K. Hopke, J. Jedelsky, and M. Jicha, "Development of a realistic human airway model," Proc Inst Mech Eng Part H J Eng Med. 226(3):197-207. doi:10.1177/0954411911430188 (2012).

[42]P. G. Koullapis, L. Nicolaou, and S. C. Kassinos, "In silico assessment of mouth-throat effects on regional deposition in the upper tracheobronchial airways," J Aerosol Sci. 117(November):164-188. doi:10.1016/j.jaerosci.2017.12.001 (2018).

[43]Y. H. Kim, Z. B. Tong , H. K. Chan, and R. Y. Yang, "CFD modelling of air and particle flows in different airway models," J Aerosol Sci. 134 (February):14-28. doi:10.1016/j.jaerosci.2019.04.015 (2019).

[44]R. L. Colasanti, M. J. Morris, R. G. Madgwick, L. Sutton, and E. M. Williams, "Analysis of tidal breathing profiles in cystic fibrosis and COPD," Chest. 125(3):901-908. doi:10.1378/chest.125.3.901 (2004).

[45]P. K. Jeffery, "Remodeling and inflammation of bronchi in asthma and chronic obstructive pulmonary disease," Proc Am Thorac Soc. 1(3):176-183. doi:10.1513/pats.200402-009MS (2004).

[46]M. Vitacca, R. Porta, L. Bianchi, E. Clini, and N. Ambrosino, "Differences in spontaneous breathing pattern and mechanics in patients with severe COPD recovering from acute excerbation," Eur Respir J. 13(2):365-370. doi:10.1183/09031936.99.13236599 (1999).

[47]A. Scheinherr, L. Bailly, O. Boiron, A. Lagier, T. Legou, M. Pichelin, G. Caillibotte, and A. Giovanni, "Realistic glottal motion and airflow rate during human breathing," Med Eng Phys. 37(9):829-839. doi:10.1016/j.medengphy.2015.05.014 (2015).

[48] B. Soni and S. Aliabadi, "Large-scale CFD simulations of airflow and particle deposition in lung airway," Comput Fluids. 88:804-812. doi:10.1016/j.compfluid.2013.06.015 (2013).

[49]K. Kuga, R. Kizuka, N. Dang, and K. Ito, "Computer Methods and Programs in Biomedicine

Effect of transient breathing cycle on the deposition of micro and nanoparticles on respiratory walls," Comput Methods Programs Biomed. 236:107501. doi:10.1016/j.cmpb.2023.107501 (2023).

[50]U. Farooq, H. H. Riaz, A. Munir, M. Zhao, A. Tariq, and M. S. Islam, "Application of heliox for optimized drug delivery through respiratory tract," Phys Fluids. 35(10). doi:10.1063/5.0169934 (2023).

[51]A. Arsalanloo, M. Abbasalizadeh, M. Khalilian, Y. Saniee, A. Ramezanpour, and M. S. Islam, "A computational approach to understand the breathing dynamics and pharmaceutical aerosol transport in a realistic airways," Adv Powder Technol. 33(7):103635. doi:10.1016/j.apt.2022.103635 (2022).

[52]K. Ahookhosh, M. Saidi, M. Mohammadpourfard, H. Aminfar, H. Hamishehkar, A. Farnoud, and O. Schmid, "Flow Structure and Particle Deposition Analyses for Optimization of a Pressurized Metered Dose Inhaler (pMDI) in a Model of Tracheobronchial Airway," Eur J Pharm Sci. 164. doi:10.1016/j.ejps.2021.105911 (2021).

[53]M. Singh, S. Basu, and D. Samanta, "Non-Newtonian fluid droplet impact dynamics on thin liquid films," Phys Fluids. 37(2). doi:10.1063/5.0252453 (2025).

[54]C. S. Kim and D. M. Fisher, "Deposition Characteristics of Aerosol Particles in Sequentially Bifurcating Airway Models," Aerosol Sci Technol. 31(2-3):198-220. doi:10.1080/027868299304255 (1999).

[55]M. R. Gorji, O. Pourmehran, M. G. Bandpy, and T. B. Gorji, "CFD simulation of airflow behavior and particle transport and deposition in different breathing conditions through the realistic model of human airways," J Mol Liq. 209:121-133. doi:10.1016/j.molliq.2015.05.031 (2015).

[56]R. Bessler, S. Bhardwaj, D. Malka, R. Fishler, J. Sznitman, "Exploring the role of electrostatic deposition on inhaled aerosols in alveolated microchannels," Sci Rep. 13(1):1-14. doi:10.1038/s41598-023-49946-w (2023).

[57]H. Liu, S. Ma, T. Hu, and D. Ma, "Computational investigation of flow characteristics and particle deposition patterns in a realistic human airway model under different breathing conditions," Respir Physiol Neurobiol. 314(June):104085. doi:10.1016/j.resp.2023.104085 (2023).

[58]P. Koullapis, B. Ollson, S. C. Kassinos, and J. Sznitman, "Multiscale in silico lung modeling

strategies for aerosol inhalation therapy and drug delivery," Curr Opin Biomed Eng. 11:130-136. doi:10.1016/j.cobme.2019.11.003 (2019).

[59]P. G. Koullapis, F. S. Stylianou, J. Sznitman, B. Olsson, and S. C. Kassinos, "Towards whole-lung simulations of aerosol deposition: A model of the deep lung," J Aerosol Sci. 144(December 2019):105541. doi:10.1016/j.jaerosci.2020.105541 (2020).